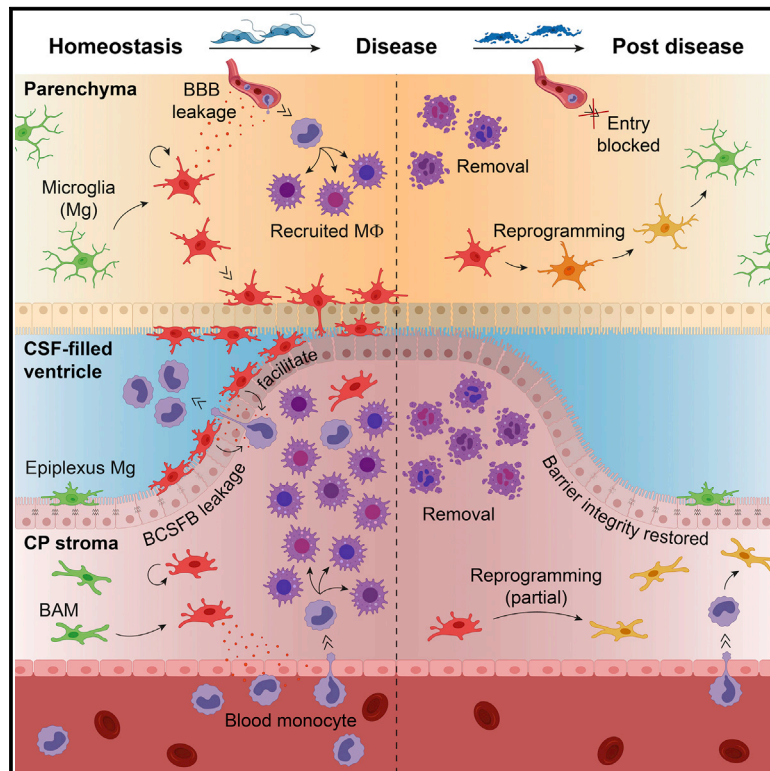


Immunity

Differential plasticity and fate of brain-resident and recruited macrophages during the onset and resolution of neuroinflammation

Graphical abstract



Authors

Karen De Vlaminc, Hannah Van Hove, Daliya Kancheva, ..., Jo A. Van Ginderachter, Roosmarijn E. Vandenbroucke, Kiavash Movahedi

Correspondence

kiavash.movahedi@vub.be

In brief

De Vlaminc et al. examine the fate of microglia, border-associated macrophages, and recruited macrophages upon *Trypanosoma brucei* infection and resolution of neuroinflammation. They show how different types of brain macrophages orchestrate the immune response to invading parasites, revealing that brain-resident and recruited macrophages exhibit diverging responses and dynamics during infection and the return to homeostasis.

Highlights

- *T. brucei* parasites invade the brain via its borders and evoke macrophage expansion
- Brain-resident and blood-recruited macrophages show divergent responses
- Upon disease resolution, recruited macrophages rapidly disappear and do not engraft
- While disease-associated microglia revert toward homeostasis, BAMs remain altered

Article

Differential plasticity and fate of brain-resident and recruited macrophages during the onset and resolution of neuroinflammation

Karen De Vlamincq,^{1,2,3} Hannah Van Hove,^{1,2,3} Daliya Kancheva,^{1,2,3} Isabelle Scheyltjens,^{1,2,3} Ana Rita Pombo Antunes,^{1,2} Jonathan Bastos,³ Monica Vara-Perez,^{1,2,3} Leen Ali,^{1,2,3} Myrthe Mampay,³ Lauren Deneuer,⁴ Juliana Fabiani Miranda,^{1,2} Ruiyao Cai,⁵ Luc Bouwens,⁶ Dimitri De Bundel,⁷ Guy Caljon,⁸ Benoît Stijlemans,^{1,2} Ann Massie,⁴ Jo A. Van Ginderachter,^{1,2} Roosmarijn E. Vandenbroucke,^{9,10} and Kiavash Movahedi^{1,2,3,11,*}

¹Myeloid Cell Immunology Laboratory, VIB Center for Inflammation Research, Brussels, Belgium

²Laboratory of Cellular and Molecular Immunology, Vrije Universiteit Brussel, Brussels, Belgium

³Laboratory for Molecular and Cellular Therapy, Vrije Universiteit Brussel, Brussels, Belgium

⁴Laboratory of Neuro-Aging & Viro-Immunotherapy, Vrije Universiteit Brussel, Brussels, Belgium

⁵Institute for Stroke and Dementia Research, Klinikum der Universität München, Ludwig-Maximilians University Munich, Munich, Germany

⁶Cell Differentiation Laboratory, Vrije Universiteit Brussel, Brussels, Belgium

⁷Department of Pharmaceutical Chemistry, Drug Analysis and Drug Information, Research Group Experimental Pharmacology, Center for Neurosciences, Vrije Universiteit Brussel, Brussels, Belgium

⁸Laboratory of Microbiology, Parasitology and Hygiene, Faculty of Pharmaceutical, Biomedical and Veterinary Sciences, University of Antwerp, Antwerp, Belgium

⁹Barriers in Inflammation Laboratory, VIB Center for Inflammation Research, Ghent, Belgium

¹⁰Ghent Gut Inflammation Group, Ghent University, Ghent, Belgium

¹¹Lead contact

*Correspondence: kiavash.movahedi@vub.be

<https://doi.org/10.1016/j.immuni.2022.09.005>

SUMMARY

Microglia and border-associated macrophages (BAMs) are brain-resident self-renewing cells. Here, we examined the fate of microglia, BAMs, and recruited macrophages upon neuroinflammation and through resolution. Upon infection, *Trypanosoma brucei* parasites invaded the brain via its border regions, triggering brain barrier disruption and monocyte infiltration. Fate mapping combined with single-cell sequencing revealed microglia accumulation around the ventricles and expansion of epiplaxus cells. Depletion experiments using genetic targeting revealed that resident macrophages promoted initial parasite defense and subsequently facilitated monocyte infiltration across brain barriers. These recruited monocyte-derived macrophages outnumbered resident macrophages and exhibited more transcriptional plasticity, adopting anti-microbial gene expression profiles. Recruited macrophages were rapidly removed upon disease resolution, leaving no engrafted monocyte-derived cells in the parenchyma, while resident macrophages progressively reverted toward a homeostatic state. Long-term transcriptional alterations were limited for microglia but more pronounced in BAMs. Thus, brain-resident and recruited macrophages exhibit diverging responses and dynamics during infection and resolution.

INTRODUCTION

To protect itself from inflammation and disease, the brain combines immune privilege with immune surveillance. From an immunological viewpoint, the brain can be considered to contain three compartments. The first compartment harbors permissive tissues containing fenestrated blood vessels that allow for blood-brain communication, CNS antigen sampling, and immune cell trafficking. This includes the dura mater, choroid plexus (CP), and circumventricular organs (Louveau et al., 2015; Mastorakos and McGavern, 2019; Rustenhoven et al., 2021). Epithelial and fibroblast barriers separate these

open regions from the next compartment, which contains the cerebrospinal fluid (CSF) that flows within the brain's ventricles. The blood-CSF barrier is thought to act as a selective gate that allows immune cell entry only under specific conditions (Shechter et al., 2013). The third and most immune-privileged compartment is the parenchyma, consisting of the brain's functional tissue. The parenchyma is shielded from the CSF by the glia limitans, an astrocyte barrier in the subdural and perivascular spaces, and by the ependyma, ciliated epithelial cells that cover the ventricles (Mastorakos and McGavern, 2019). Furthermore, blood endothelial cells within the subdural space and the parenchyma contain tight junctions, forming

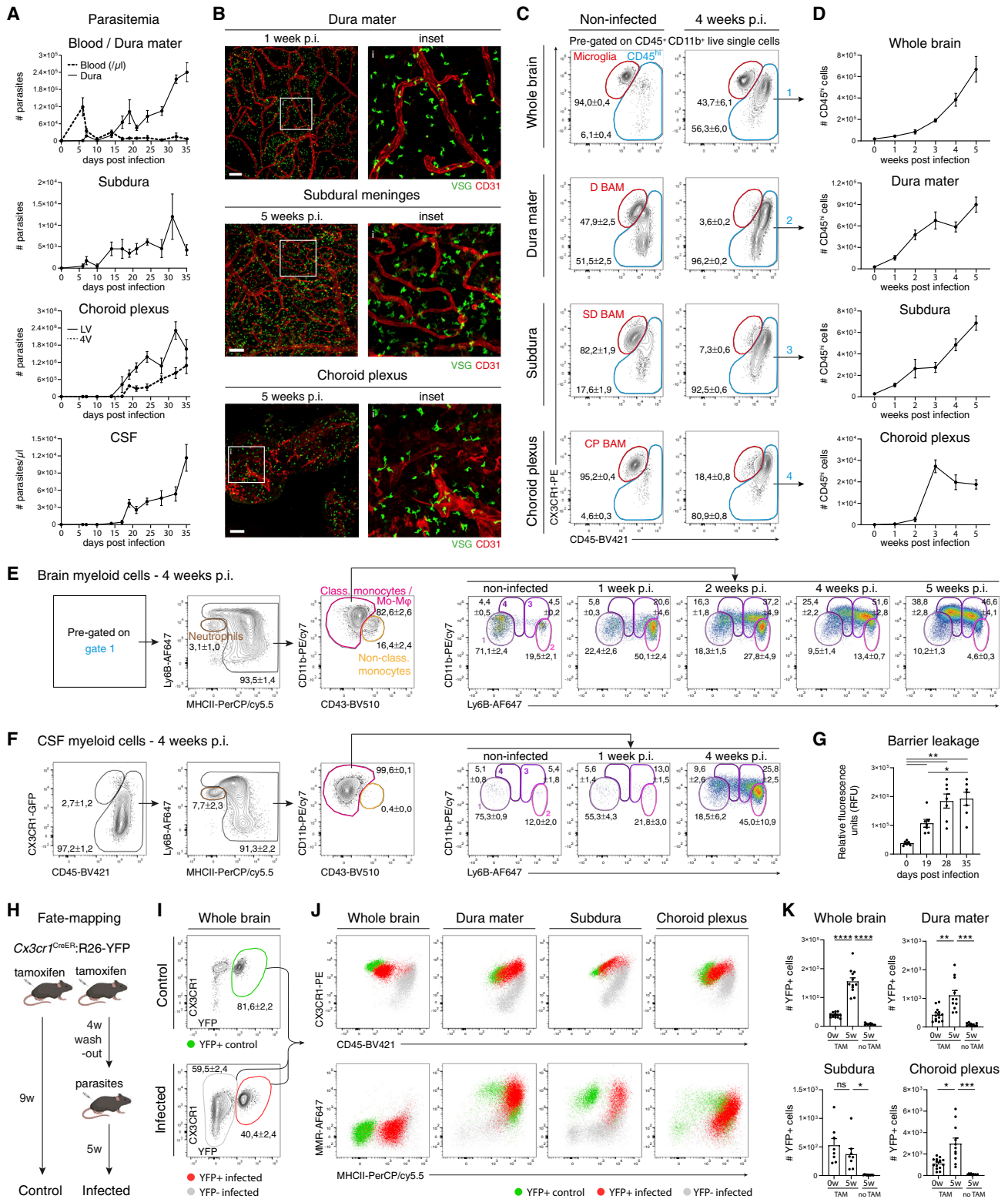


Figure 1. *T. b. brucei* parasites invade the brain via its border regions and trigger the recruitment of monocyte-derived cells

(A) Parasitemia in blood and brain regions of C57BL/6 mice during infection. Mean \pm SEM of $n = 4-8$ mice/time point from 2 independent experiments.

(B) Whole mount of dura and subdura, and coronal section of lateral ventricle CP. Parasites and blood vessels stained with anti-VSG and anti-CD31, respectively. $n = 4-5$ mice. Scale bars: 100 μ m (dura/subdura) or 75 μ m (CP).

(legend continued on next page)

the blood-leptomeningeal and blood-brain barrier, respectively. The blood-accessible border regions of the brain contain a diverse immune repertoire, while the immune-privileged parenchyma primarily hosts macrophages (Mrdjen et al., 2018; Van Hove et al., 2019).

Tissue-resident macrophages have emerged as key regulators of brain development, homeostasis, and disease (Kierdorf et al., 2019; Prinz et al., 2019). Resident macrophages within the brain parenchyma are known as microglia, while those in non-parenchymal tissues are called border-associated macrophages or BAMs. They are derived from early yolk sac progenitors that seed the mouse brain around E9.5 (Ginhoux et al., 2010; Utz et al., 2020). While microglia, subdural BAMs, and perivascular BAMs remain of embryonic origin, a fraction of BAMs in the dura and CP stroma are replaced by adult monocytes throughout life (Goldmann et al., 2016; Van Hove et al., 2019). Microglia and BAMs exhibit distinct transcriptional profiles, with non-overlapping expression of many signature genes, including *Sall1*, *P2ry12*, and *Sparc* in microglia and *Ms4a7*, *Tgfb1*, and *Clec12a* in BAMs (Van Hove et al., 2019). Single-cell analysis has started to unveil brain macrophage heterogeneity and their responses upon disease. This has primarily been assessed for microglia, leading to the identification of a disease-associated microglia (DAM) state that was first observed in mouse models of neurodegeneration (Keren-Shaul et al., 2017), and subsequently in many other settings (Anderson et al., 2019; Hammond et al., 2019; Jordão et al., 2019; Li et al., 2019; Masuda et al., 2019; Safaiyan et al., 2021; Van Hove et al., 2019). However, the responses of BAMs during disease remain to be further defined. Disease can also result in the recruitment of monocytes into the various brain compartments. The degree to which recruited macrophages molecularly and functionally differ from resident microglia and BAMs remains incompletely understood. Resolving this requires single-cell analysis combined with fate mapping approaches. Furthermore, the fate of resident and recruited macrophages upon disease resolution remains largely unexplored.

Here, we studied brain macrophage responses during mouse infections with the brain-invading unicellular parasite *Trypanosoma brucei*. This flagellated extracellular parasite consists of three subspecies. *T. b. rhodesiense* and *T. b. gambiense* infect humans and cause African trypanosomiasis or sleeping sickness (Kennedy and Rodgers, 2019). *T. b. brucei* is unable to infect hu-

mans, but infections in mice serve as a good model for the human disease (Magez and Caljon, 2011). *T. brucei* infections occur when its vector, the tsetse fly, takes a blood meal, whereupon parasites move from the dermis to the draining lymph node and blood (Caljon et al., 2016). Through antigenic variation of its variant surface glycoprotein (VSG) coat (Stijlemans et al., 2016), parasites are able to persist and move into peripheral organs and the brain (Kristensson et al., 2010). Without treatment, humans and mice eventually die from the infection, with final stages of the human disease being characterized by sleep dysregulation and neurological dysfunctions (Kristensson et al., 2010). Here, we show that *T. b. brucei* invaded the mouse brain in a stepwise fashion by progressively moving across its three compartments (border regions, CSF, and parenchyma). This induced an extensive meningoencephalitic response coupled to a massive mobilization of both resident and recruited macrophages. By combining serial two-photon tomography, fate mapping, single-cell RNA sequencing, and genetic ablation, we delineate the transcriptional dynamics and functional diversity of microglia, BAMs, and recruited macrophages during parasite infection, and we uncover their fate following drug-induced resolution of disease.

RESULTS

Trypanosoma brucei invades the brain via stepwise infiltration of its border regions, triggering the disruption of brain barriers and the recruitment of peripheral myeloid cells

Intraperitoneal inoculation of mice with *T. b. brucei* results in a systemic infection to which all animals succumb at around 5 weeks post injection (p.i.) (Stijlemans et al., 2014). Parasites initially expand strongly in the blood but are then controlled through an adaptive immune response, which triggers trypanosomal antigenic variation and immune escape (Stijlemans et al., 2016). In humans, *T. brucei* infection eventually develops into a fatal neurological disease, but the kinetics and the route of brain infection remain unclear. Using the mouse model, we assessed the kinetics of brain infection by quantifying parasites in the brain's border regions, CSF, and parenchyma over time. Blood parasitemia in infected mice peaked at day (d) 6 p.i., followed by a second smaller peak at d14, after which parasite numbers remained low (Figure 1A). In the brain, parasites were

(C) Flow cytometry on myeloid cells, pre-gated on CD45⁺CD11b⁺ live single cells. Brain-resident macrophages shown in red (CX3CR1^{hi}CD45^{lo-int}), blood-recruited cells in blue (CD45^{hi}). In enriched subdura, microglia were prior out-gated as shown in Figure S1D. n = 4–5 mice/time point, representing 2 independent experiments.

(D) CD45^{hi} myeloid cell kinetics over time. Mean ± SEM of n = 9–10 mice/time point from 2 independent experiments.

(E and F) Identification of CD45^{hi} myeloid cells in infected whole brain (E) and CSF (F) (left), and kinetics of classical monocyte-to-macrophage differentiation over the course of infection (right). Results in (F) of n = 3 with 4 mice/sample/time point.

(G) Relative fluorescence in CSF of naive and infected mice, i.v. injected with FITC-dextran 15 min prior to sacrifice. Mean ± SEM of n = 6–7 mice/time point, representing 2 independent experiments.

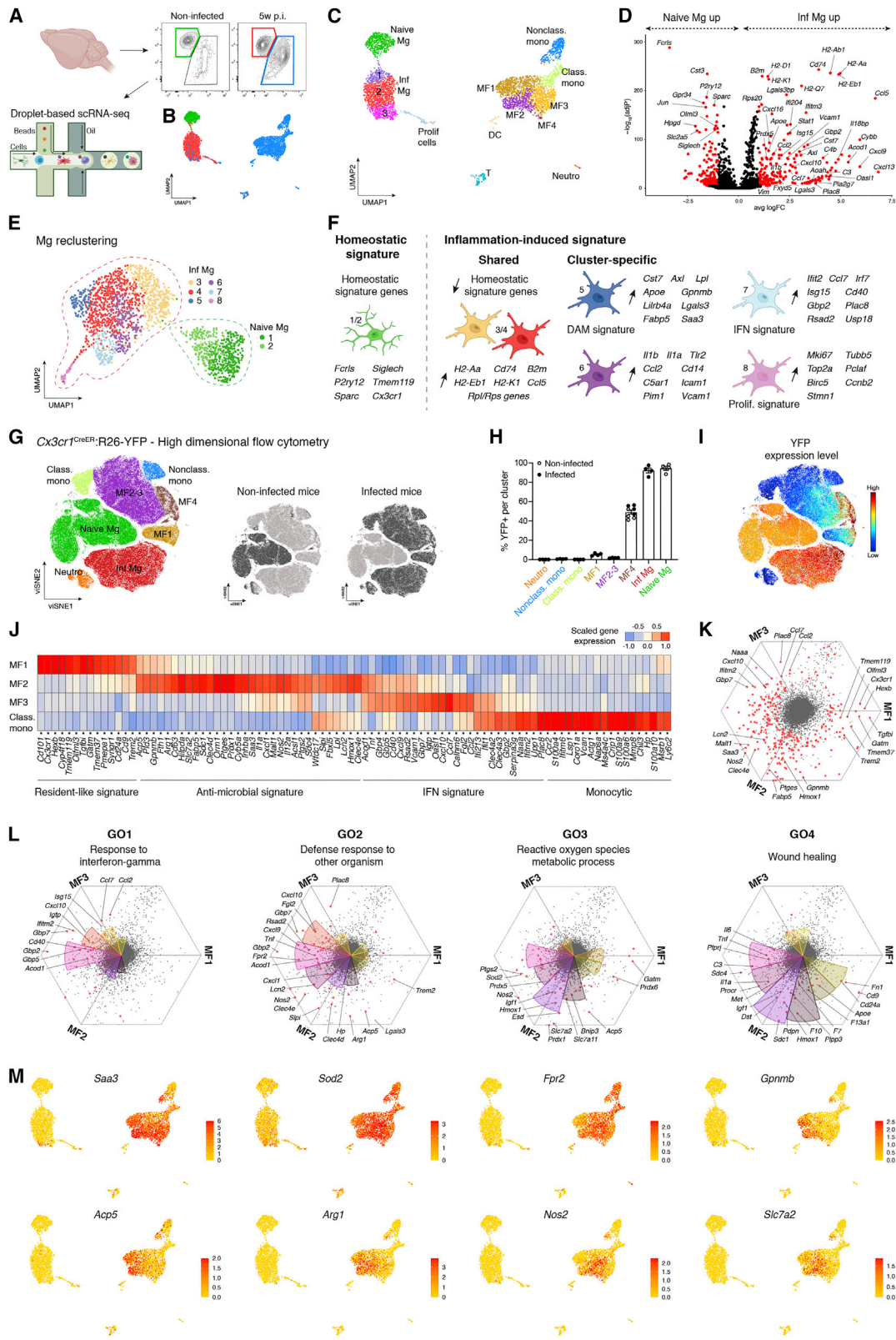
(H) Schematic representation of fate mapping in *Cx3cr1*^{CreER};R26-YFP mice.

(I) YFP expression of brain myeloid cells (gated as live single CD45⁺CD11b⁺). Resident macrophages (YFP⁺) indicated in green (control) or red (infected), YFP⁻ cells in gray (infected).

(J) Marker expression of YFP⁺ and YFP⁻ cells as gated in (I). Results in (I) and (J) represent 2–4 independent experiments with n = 8–14 mice/group.

(K) YFP⁺ myeloid cell numbers in brain and borders; tamoxifen-naive mice served as control. Mean ± SEM of n = 8–14 mice/group from 2–4 independent experiments. Significance in (G) and (K) evaluated by Dunnett's T3 multiple comparisons test, ns, *p < 0.05, **p < 0.01, ***p < 0.001, ****p < 0.0001. Statistics, Table S3.

See also Figure S1.



(legend on next page)

detected in the dura mater at d7 p.i. (Figure 1A) and immunostaining revealed their extravasation into the connective tissue (Figure 1B). Parasite numbers in the dura progressively increased toward d35 p.i., contrary to what was observed in the blood. A comparable kinetic was observed in the subdural meninges (Figures 1A and 1B). In the CP, no parasites were detected during the first 2 weeks of infection, but their numbers rapidly expanded upon their arrival in the lateral and fourth ventricle CP (Figure 1A), where they were observed in the stromal tissue (Figure 1B). Shortly after CP colonization, CSF parasitemia strongly increased and peaked at the end stage of disease (Figure 1A). Parenchymal infiltration was further delayed, with a surge in hippocampal parasitemia around 3 weeks p.i. (Figures S1A and S1B). Extravasated parasites could also be observed in other parenchymal regions, for example in periventricular areas (Figure S1A). Together, this shows that *T. brucei* has a strong propensity to accumulate in the brain's border regions, moving from the meninges to the CP, CSF, and parenchyma.

Concurrent with parasite invasion, we observed a strong infiltration of CD45^{hi} blood-recruited myeloid cells in the brain. In naive mice, microglia and BAMs were identified as CD11b⁺CX3CR1^{hi}CD45^{lo} and CD11b⁺CX3CR1^{hi}CD45^{int} myeloid cells, respectively (Figure 1C) (Van Hove et al., 2019). These resident macrophages lost their relative abundance to CD11b⁺CD45^{hi} myeloid cells that progressively accumulated in whole brain samples and dissected brain regions (Figures 1C, 1D, S1C, and S1D). The majority of CD11b⁺CD45^{hi} cells were mononuclear cells consisting of Ly6B^{lo}CD43⁺ non-classical monocytes, Ly6B^{hi}CD43⁻ classical monocytes and monocyte-derived macrophages at various stages of differentiation (Figures 1E and S1E). Infiltrating monocytes gradually lost their Ly6B expression, revealing their differentiation into CD11b^{hi}Ly6B^{lo} macrophages that accumulated as the disease progressed (Figures 1E and S1E). We also observed a strong increase in the number of myeloid cells in the CSF at later stages of infection. CSF myeloid cells consisted of neutrophils and MHCII⁺CD43⁻ cells, most of which expressed high levels of Ly6B (Figures 1F and S1F), indicative of activated classical monocytes. Non-classical monocytes were virtually absent, suggesting that these cells do not traffic via the CSF. Corresponding to the immune influx, many pro-inflammatory cyto-

kines and chemokines were significantly increased in the CSF upon infection, including a strong induction of the monocyte chemoattractants CCL2 and CCL5 (Figure S1G). Furthermore, intravenously injected fluorescent dextran revealed increasing relative fluorescence in the CSF of infected mice (Figure 1G), indicating a progressive elevation of blood-CSF barrier permeability. At late stages of disease, leakage was also observed in the brain parenchyma (Figure S1H), suggestive of local blood-brain barrier disruption.

The CD11b⁺CD45^{hi} myeloid cell gate may not only constitute recruited cells but could also contain resident macrophages that upregulated CD45 expression upon inflammation. To unequivocally distinguish resident versus recruited brain macrophages, we relied on fate mapping (Figure 1H). *Cx3cr1*^{CreER};R26-YFP mice received tamoxifen injections to induce reporter labeling in brain macrophages. 4 weeks later, when YFP labeling is lost in monocytes (Goldmann et al., 2013; Yona et al., 2013), mice were infected, allowing us to distinguish long-lived resident brain macrophages (YFP⁺) from recruited monocyte-derived cells (YFP⁻). YFP⁺ microglia and BAMs could be identified in whole brain samples and dissected border regions via flow cytometry (Figures 1I and S1I). While microglia and BAMs indeed upregulated CD45 expression during infection (Figure 1J), their contribution to the CD11b⁺CD45^{hi} population was minor (Figure S1J), indicating that the majority of CD11b⁺CD45^{hi} cells that accumulate during infection are newly recruited. Yet, quantification of the absolute number of YFP⁺ cells showed that microglia and BAMs in the dura and CP also expanded during infection (Figure 1K). In the absence of tamoxifen treatment, the number of YFP⁺ brain myeloid cells was negligible, verifying that the increase in YFP⁺ cells was not due to leaky excision (Van Hove et al., 2020) in recruited macrophages. To confirm that pre-existing YFP⁺ BAMs expanded, we performed Ki67 staining on dural wholemounts, which revealed an increase in the number of proliferating Ki67⁺YFP⁺ BAMs during infection (Figure S1K).

Recruited brain macrophages adopt distinct inflammatory states as compared with activated resident microglia

To study transcriptional changes in parenchymal microglia during infection and to compare their gene signatures with those of recruited macrophages, we performed single-cell RNA

Figure 2. Microglia and recruited brain macrophages adopt distinct activation states

- (A) Schematic overview of scRNA-seq setup used on FACS sorted whole brain myeloid cells of naive and infected C57BL/6 mice. n = 4 mice/group (pooled).
(B) UMAP of 4,557 cells, color-coded according to sorted populations in (A).
(C) Cluster identification.
(D) Volcano plot (VP) showing differentially expressed (DE) genes (red, $-\log_{10}(\text{adjP}) > 5$, $\text{abs}(\log_2\text{FC}) > 1$) between microglia from infected and naive mice.
(E and F) Reclustered microglia, revealing subsets with distinct gene signatures.
(G) Flow cytometry viSNE, showing 2×10^5 brain myeloid cells of non-infected and infected *Cx3cr1*^{CreER2};R26-YFP mice. n = 4 mice/group representing 2 independent experiments. Clusters were identified based on marker expression (Figure S2E) and colored according to their counterparts in scRNA-seq (C). Sample origin is highlighted in dark gray.
(H and I) Cluster distribution of YFP⁺ cells (H) and YFP expression levels (I).
(J) Heatmap with scaled expression of selected marker genes in classical monocytes and recruited MF clusters in (C).
(K and L) Directional distribution of all gene transcripts in MF1–3. In red: all DE genes ($-\log_{10}(\text{adjP}) > 5$, $\text{abs}(\log_2\text{FC}) > 0.5$) (K) or only the DE genes enriched for given top GO terms (L). Distance and direction from the center is a measure for each transcript's scaled average expression in MF1–3. Circle sector areas in (L) denote the relative number of DE genes in a particular direction for given GO term.
(M) UMAPs highlighting expression differences between microglia and recruited macrophages for various inflammation-associated genes.
See also Figure S2 and Table S1.

sequencing (scRNA-seq) on CD11b⁺CD45⁺ myeloid cells that were sorted from naive and infected mice (Figure 2A). The samples were combined in a single dataset followed by uniform manifold approximation and projection (UMAP) embedding. Microglia, which were identified as *Sall1*⁺*Sparc*⁺*C1qb*⁺ clusters (Figure S2A), segregated in naive versus infected brains (Figures 2B and 2C), indicating a globally altered transcriptional state. When comparing microglia from infected (Inf Mg) and naive mice (Naive Mg), we observed a downregulation of homeostatic genes (*Fcrls*, *Sparc*, and *P2ry12*) (Butovsky et al., 2014; Gautier et al., 2012; Hickman et al., 2013) and an upregulation of inflammation-associated genes in Inf Mg (Figures 2D and S2A). This included a strong induction of MHCII transcripts (*H2-Aa* and *Cd74*), which were uniformly expressed in all microglia from infected mice (Figure S2A). Microglia were then reclustered to further explore their heterogeneity (Figure 2E). This revealed typical DAM genes (*Apoe*, *Cst7*, and *Lilrb4a*) in cluster 5, pro-inflammatory factors (*Il1b*, *C5ar1*, and *Ccl2*), immune sensors (*Cd14* and *Tlr2*) and the *Icam1* and *Vcam1* adhesion molecules in cluster 6, and an interferon-induced gene signature (*Ifit2*, *Isg15*, and *Rsad2*) in cluster 7 (Figures 2F and S2B). Cluster 8 represented proliferating microglia (*Mki67*, *Top2a*, and *Birc5*), which is in line with microglial expansion (Figure 1K).

In addition to microglia, we identified non-classical monocytes (*Ear2*⁺*Spn*⁺*Ace*⁺), classical monocytes (*Ccr2*^{hi}*Chil3*^{hi}*S100a4*^{hi}), and four clusters of *Sall1*⁻*Sparc*⁻*C1qb*^{hi} macrophages (MF1–4) (Figures 2C and S2A). Clusters MF1–MF3 exhibited high expression of *Ly6c2* and *Clec12a*, while this was lower in MF4 (Figure S2C). In contrast, MF4 showed an enriched expression of *Ccl8*, *Vcam1*, and *Cp*, which are signature genes for BAMs (Van Hove et al., 2019) (Figure S2C). MF1 exhibited an upregulation of typical microglia genes, such as *Tmem119*, *Olfml3*, and *Cd9* (Figure S2C), although their expression levels remained substantially lower than in microglia (Figure S2A). This could suggest a modest degree of imprinting by the brain microenvironmental niche in recruited macrophages. However, we cannot exclude that this cluster represents microglia that had converted. To obtain insights into the ontogeny of these macrophage populations, we combined fate mapping in *Cx3cr1*^{CreER}:R26-YFP mice with high-dimensional flow cytometry. We relied on our scRNA-seq data to design a flow cytometry panel that could differentiate between the various macrophage subsets (Figure S2D) and found that the main macrophage populations that were identified via scRNA-seq could also be mapped onto the flow analysis (Figures 2G and S2E). This revealed that the vast majority of macrophages corresponding to MF1 did not exhibit YFP expression (Figures 2H and 2I), arguing against a microglial origin. YFP expression was observed in the F4/80^{hi}Ly6C^{lo}CLEC12A^{lo} macrophages that corresponded to MF4 (Figures 2H, 2I, and S2E). This indicates that MF4 is derived from resident BAMs, while MF1–3 represent recruited macrophages.

Gene ontology (GO) enrichment revealed that some of the recruited macrophages exhibited a prominent expression of genes involved in antimicrobial responses (Figure 2J). To visualize the relevant gene expression modules across the three clusters, we plotted all detected transcripts in hexagonal diagrams (Figure 2K). For each gene, the direction and distance from the origin is a measure for its upregulation in any of the 3 clusters. GO term analysis showed an IFN-induced response

(GO1) in MF3 (Figure 2L; Table S1). Antimicrobial defense response (GO2) was prominent in both MF2 and MF3, and GO terms related to production of reactive oxygen/nitrogen species (GO3), and tissue-remodeling (GO4) were skewed toward MF2 (Figure 2L; Table S1), suggesting that these cells play a key role in parasite control. Many of the inflammatory genes found in recruited monocyte-derived macrophages, including *Nos2*, *Arg1*, *Slc7a2*, and *Acp5*, were hardly expressed in activated microglia (Figures 2M and S2F), suggesting a differential role for pre-existing and newly recruited macrophages in response to infection.

Spatial mapping of resident and recruited macrophages reveals an accumulation of microglia-like cells at the blood-CSF interface of the choroid plexus

To spatially map the recruited myeloid cells throughout the brain parenchyma, we relied on serial two-photon tomography (Ragan et al., 2012) in *Ly2*^{GFP} mice. The *Ly2*^{GFP} strain allows for the visualization of peripheral myeloid cell infiltration in the brain, since recruited myeloid cells exhibited high GFP expression, while microglia remained GFP⁻, as confirmed via flow cytometry (Figure S3A). BAMs however also express *Ly2* (Van Hove et al., 2019) and will be GFP⁺. 3D reconstruction revealed bright intrinsic GFP fluorescence in the brains of late-stage infected mice (Figure 3A). The accumulation of GFP^{bright} myeloid cells was evident throughout the meninges (Figure 3A), which we confirmed via whole-mount staining of the dura and pia mater of infected *Ly2*^{GFP} mice (Figure S3B). GFP^{bright} myeloid cell infiltration and/or local expansion was also prominent in and around the CP and in various parenchymal brain regions (Figure 3A). To assess GFP^{bright} parenchymal cell distribution in more detail, each of the 300+ brain sections was mapped onto the Allen brain atlas and the number of GFP^{bright} pixels was quantified for individual regions (Figures S3C and S3D; Table S2). Substantial myeloid cell infiltration was observed in all circumventricular organs, which are parenchymal brain regions containing fenestrated vessels (Figures S3C and S3D). Several regions in the hypothalamus showed high infiltration as well, including the periventricular hypothalamic nucleus, ventrolateral preoptic nucleus and arcuate hypothalamic nucleus, which are known to be involved in sleep regulation (Obal and Krueger, 2004) and are located near the suprachiasmatic nucleus, the central regulator of circadian rhythms (Saper et al., 2005). Notable infiltration was also observed in the cerebral nuclei, including the septofimbrial nucleus, which is located around the lateral ventricle. Other hotspots of parenchymal infiltration were observed in the cerebral cortex (e.g., hippocampus), thalamus and midbrain (e.g., superior colliculus) (Figures S3C and S3D).

To specifically study resident macrophages *in situ*, we again relied on fate mapping in *Cx3cr1*^{CreER}:R26-YFP mice. YFP⁺ BAMs in the dura and subdura adopted a reactive morphology and were found throughout the tissue (Figures 3B, 3C, and S3E). Interestingly, the CP of infected mice exhibited profound swelling, with *Iba1*⁺YFP⁻ recruited myeloid cells accumulating in the CP stroma, while YFP⁺ macrophages were abundantly observed on the apical surface of the cytokeratin-stained epithelium (Figure 3D). This highlights a segregation between resident and recruited macrophages at the blood-CSF interface formed by the CP epithelial cells. In infected *Ly2*^{GFP} mice,

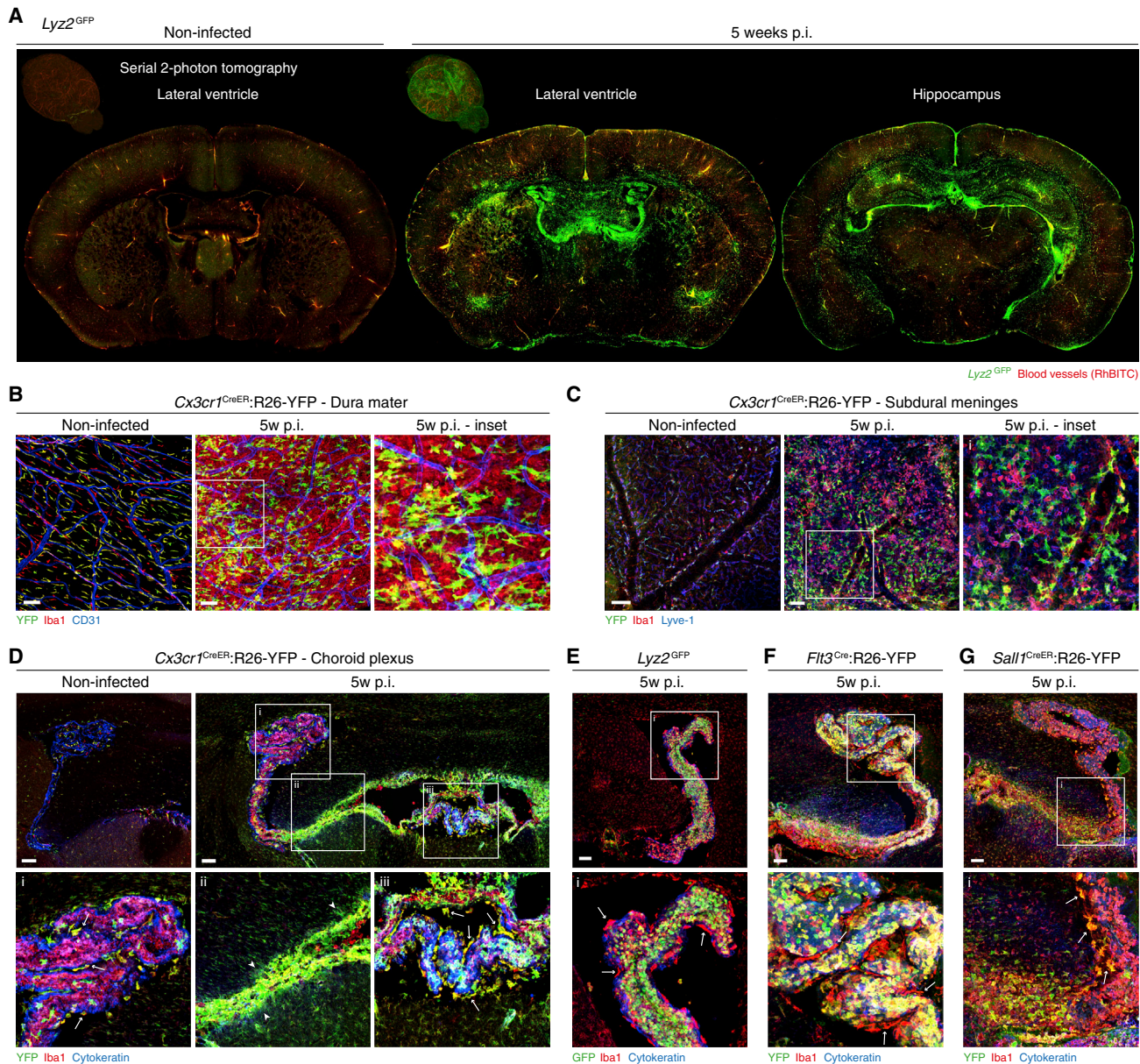


Figure 3. Spatial mapping reveals the dynamics of recruited and resident macrophages during infection and uncovers the expansion of microglia-like cells on the apical surface of the CP epithelium

(A) 3D reconstruction following serial two-photon tomography of *Lyz2^{GFP}* mouse brains and coronal sections at lateral ventricle and hippocampus. Blood-recruited myeloid cells are GFP^{bright} (green), vasculature is shown in red. Representing n = 1 non-infected and n = 3 infected mice.

(B–D) Whole mount of dura (B) and subdura (C) and coronal sections of lateral ventricle CP (D) of *Cx3cr1^{CreER}:R26-YFP* mice, stained for indicated markers. Resident BAMS are YFP⁺.

(E–G) Coronal sections of lateral ventricle CP of *Lyz2^{GFP}* (E), *Flt3^{Cre}:R26-YFP* (F), and *Sall1^{CreER}:R26-YFP* (G) mice. Green cells represent blood-recruited myeloid cells in *Lyz2^{GFP}* mice, bone-marrow-derived cells in *Flt3^{Cre}:R26-YFP* mice and microglia in *Sall1^{CreER}:R26-YFP* mice. Cells located on the apical side of the CP are *Lyz2⁻Flt3⁻Sall1⁺* (white arrows in D–G), similar to parenchymal microglia. Arrow heads in (D) highlight microglia accumulation at the ependymal lining. Images in (B)–(G) represent n = 3–5 mice. Scale bars, 100 μ m.

See also Figure S3.

Iba1⁺GFP⁺ myeloid cells were observed in the stroma, while apical macrophages were GFP⁻, similar to the surrounding parenchymal microglia (Figure 3E). We have previously shown that macrophages residing on the apical surface of the CP epithelium, known as CP^{epi} BAMS or Kolmer’s epiplexus cells,

are a sparse microglia-like population (Van Hove et al., 2019). In contrast to stromal CP BAMS, CP^{epi} BAMS are derived from embryonic *Sall1⁺* cells and receive no monocyte input (Van Hove et al., 2019). Macrophages accumulating on the CP epithelium of infected mice had an embryonic origin, as they

showed no YFP labeling in *Flt3^{Cre}:R26-YFP* mice (Figure 3F). Additionally, they were derived from *Sall1⁺* cells as shown by fate mapping using the *Sall1^{CreER}:R26-YFP* strain (Figure 3G). Flow cytometry confirmed that *Sall1*-derived cells significantly increased in the CP of infected mice (Figures S3F and S3G). This embryonic *Sall1⁺* origin suggests that during infection, the CP epithelial surface remains populated by a microglia-like population that expands in numbers. Furthermore, we also observed that in periventricular regions, microglia accumulated at the ependymal layer (Figure 3D). Adhesion molecules, such as ICAM1, are expressed on CP epithelium and are involved in leukocyte transmigration (Steffen et al., 1996; Engelhardt et al., 2001). In healthy mice, ICAM1 exhibited a patchy expression pattern on CP epithelial cells and was not observed in the ependymal layer (Figure S3H). Upon infection, ICAM1 expression completely covered the CP epithelial surface and the ependymal lining of the ventricles. CP^{epi} BAMs and microglia at the ependymal lining co-localized with this ICAM1-positive layer (Figure S3H), suggesting its involvement in macrophage trafficking across the ependymal and CP epithelial surfaces.

Fate mapping combined with single-cell sequencing validates the presence of microglia-like cells at the CP and confirms the transcriptional divergence between resident and recruited macrophages

To confirm that *Sall1⁺* macrophages at the CP of infected mice resembled microglia, we combined fate mapping in *Cx3cr1^{CreER}:R26-YFP* mice with scRNA-seq (Figure 4A). CD11b⁺CD45⁺ myeloid cells from the dissected CP primarily consisted of classical and non-classical monocytes and various clusters of *Fcgr1⁺Mafb⁺* macrophages (MF1-8) (Figures 4B and S4A). MF1-5 cells clustered adjacent to classical monocytes and the gradual reduction of *Ly6c2* and *Ccr2* and increase of complement genes (*C1qb*) indicated an ongoing monocyte-to-macrophage differentiation (Figure S4B). MF6 cells were *Mafb^{hi}C1qb^{hi}* but also expressed non-classical monocyte genes (*Ace*, *Eno3*, and *Spn*), suggesting that these are macrophages derived from non-classical monocytes. Cluster MF-EP expressed both macrophage and epithelial cell markers (Figure S4A), potentially representing cell doublets or macrophages that ingested epithelial cell fragments. Clusters MF7 and MF8 exhibited YFP expression (Figures 4C and 4D), indicative of a resident macrophage identity. To corroborate this, we pooled our data with a scRNA-seq dataset containing CP immune cells from homeostatic mice (Van Hove et al., 2019) and performed Harmony integration (Korsunsky et al., 2019). This showed that MF7 and MF8 cells clustered near stromal CP BAMs and CP^{epi} BAMs, respectively, while MF1-MF6 had no counterparts in the naive CP (Figure 4E). Furthermore, MF8 expressed *Sall1* and other microglial signature genes (*Sparc*, *P2ry12*, and *Siglech*) (Figures 4F and 4G), while MF7 expressed typical stromal BAM genes (*Ms4a7*, *Clec12a*, and *Tgfb1*) (Figure S4C). This confirms the expansion of a resident *Sall1⁺* microglia-like population at the CP of infected mice, which we will refer to as epiplexus microglia. Both MF7 and MF8 showed a clear inflammatory signature when compared with their naive counterparts, including an upregulation of *Ccl8*, *C3*, and *Cxcl13* in

stromal BAMs (Figure S4D), and MHCII and chemokine genes in epiplexus microglia (Figure S4E).

Many of the genes that were differentially up- or downregulated in CP BAMs upon infection were shared with newly recruited macrophages (Figure S4F). However, MF1-6 showed many additional differentially expressed genes that were not observed in resident macrophages. This included an upregulation of inflammatory genes such as *Nos2*, *Inhba*, *Ptges*, and *Sdc1* in MF3, *Igf1*, *Arg1*, *Fabp5*, and *Acp5* in MF4 and *Clec4b1*, *Cxcl14*, *Lpl*, and *Cadm1* in MF5 (Figures 4H and S4G). Taken together, these results show that, even within one anatomically defined region (the CP), resident macrophages and newly recruited monocyte-derived cells do not converge toward common inflammatory cell states in diseased tissue microenvironments, possibly reflecting a restricted plasticity of resident macrophages.

Resident macrophages drive a pro-inflammatory response, promoting brain barrier permeability and the recruitment of peripheral immune cells

To investigate the functional relevance of resident brain macrophages during infection, we aimed to specifically deplete these cells during infection and assess the consequences in the time window prior to their repopulation. Hereto, *Cx3cr1^{CreER}:R26-DTR* mice were infected 4 weeks after receiving tamoxifen, when diphtheria toxin receptor (DTR) expression is restricted to resident brain macrophages (DTR+) (Bruttger et al., 2015). Tamoxifen-naive littermates served as controls (DTR-) (Figure 5A). In DTR+ mice, DT injections resulted in an efficient depletion of resident macrophages throughout the infected brain, while recruited cells were spared (Figures S5A and S5B). Consequences of the depletion were first assessed during the initial 2 weeks of infection, prior to parasite infiltration in the CP. Hereto, mice received three consecutive bolus injections of DT starting from d7 p.i. and were analyzed at d10. Macrophage depletion resulted in a significant increase of parasites in the dura (Figures 5B and S5C), suggesting that resident BAMs are important for parasite control during the initial stage of the disease when parasites first enter the meninges. There was also a significant increase in the number of immune cells infiltrating the dura (Figure 5C), which may reflect a compensatory immune response to the surge in parasite numbers. However, no significant changes in fluorescent dextran leakage into the CSF or in CSF immune infiltrate were observed at this point (Figures 5D and S5D). Next, we assessed the consequence of resident macrophage depletion at later stages of disease, when parasites and immune cells have infiltrated the CP and CSF. At this point, the depletion no longer significantly affected parasite numbers in the brain (Figures 5E and S5E), suggesting that when the number of recruited myeloid cells is high, the direct involvement of resident brain macrophages in parasite control is redundant. We did, however, observe a significant reduction in fluorescent dextran leakage into the CSF of DTR+ mice (Figure 5F), and a drop in the number of CSF-infiltrating immune cells, reflecting a reduction in both myeloid cells and lymphocytes (Figure 5G). In line with this, CSF concentrations of the chemokines CCL5 and CXCL1 were significantly decreased

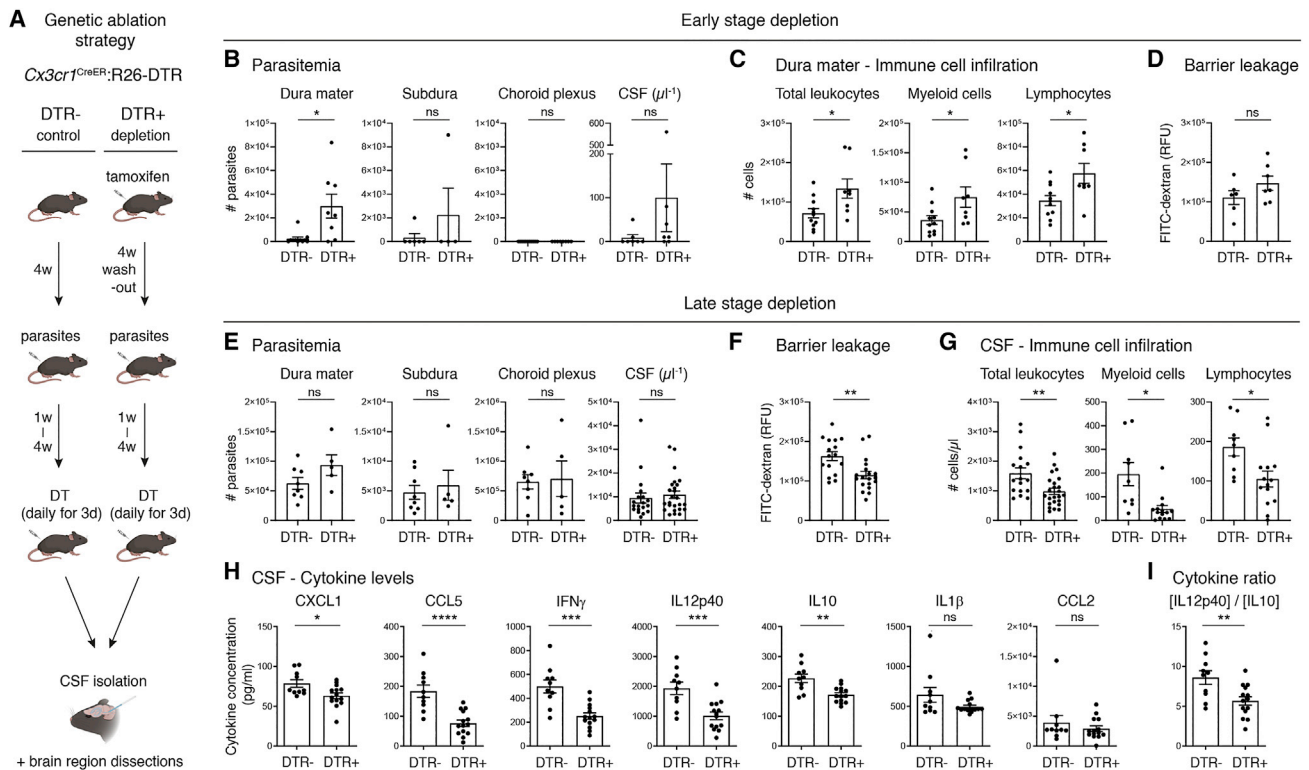


Figure 5. Genetic ablation of resident macrophages impairs initial parasite control but reduces brain barrier permeability and the recruitment of peripheral immune cells at later stages of disease

(A) Schematic representation of brain-resident macrophage ablation in *Cx3cr1^{CreER};R26-DTR* (DTR+) mice; tamoxifen-naïve littermates were used as DTR- controls.

(B–D) Depletion at early stage of disease, prior to parasite infiltration into CP (sacrificed d10 p.i.). Effect shown on parasitemia (B), on immune infiltration in dura mater (C), and on blood-CSF barrier leakage (D). $n = 4–11$ mice/group from 2–3 independent experiments.

(E–I) Depletion at later stages of disease. Effect on parasitemia (sacrificed d30 p.i., [E]), on blood-CSF barrier leakage (d24 p.i., [F]), on CSF immune infiltration (manual count for total leukocytes, FACS count for others) (d30 p.i., [G]), and on CSF cytokine levels (d30 p.i., [H and I]). $n = 5–25$ mice/group from 2 to 4 independent experiments. Graphs show mean \pm SEM, significance was evaluated by unpaired t test (Welch's correction when appropriate), ns, * $p < 0.05$, ** $p < 0.01$, *** $p < 0.001$, **** $p < 0.0001$. Statistics, Table S3.

See also Figure S5.

Upon disease resolution recruited macrophages are rapidly removed and do not engraft as resident macrophages

Melarsoprol is an arsenical that is used to treat late-stage human trypanosomiasis and clears parasites from infected mice (Burrell-Saward et al., 2015). To study the fate of the brain myeloid compartment upon disease resolution, mice received a curative treatment with melarsoprol at 4 weeks p.i. (Figure S6A). Upon melarsoprol treatment, brain barrier integrity was quickly restored (Figure S6B). Additionally, the CD45^{hi} myeloid cells that had infiltrated the brain and its border regions rapidly disappeared (Figures 6A and 6B), with 75%–90% of these cells being lost within a week (Figure S6C). To determine whether this was linked to cell death, we assessed annexin V and propidium iodide (PI) staining during the initial 60 h post melarsoprol treatment via flow cytometry. Even prior to drug treatment, the CD45^{hi} myeloid gate contained $21.7\% \pm 1.6\%$ AnnexinV⁺PI⁻ and $5.7\% \pm 1.2\%$ AnnexinV⁺PI⁺ cells, which represent early and late apoptotic cells, respectively (Figure S6D). These percentages were substantially higher than what was observed for microglia (Figures S6D and S6E). Additionally, the percentage

of AnnexinV⁺PI⁺ CD45^{hi} myeloid cells significantly increased at 12 h post melarsoprol treatment. Together, these results suggest that recruited macrophages are short-lived cells that are quickly removed from the brain upon disease resolution.

To map the transcriptional changes in recruited macrophages upon disease resolution, we performed scRNA-seq on $\text{CD45}^{\text{+}}\text{CD11b}^{\text{+}}$ myeloid cells from brains of infected mice at d28 p.i. (cured d0) and cured mice at d3, d7, d9, and d57 post melarsoprol treatment. The samples were combined in a single dataset and non-microglial cells were selected and separately analyzed (Figure 6C). Classical monocytes and monocyte-derived macrophages that were present at d0 (cM1 and MF1), clustered separately from their counterparts observed at d3 (cM2 and MF2) (Figure 6D). The expression of inflammatory genes was reduced in clusters cM2 and MF2, and these cells exhibited a strong interferon-induced gene signature (Figures 6E and S6F), which may be a response to sudden widespread parasite death. Clusters cM2 and MF2 gradually disappeared over time (Figures 6D and 6F). Conversely, macrophages with a resident BAM signature (MF3) persisted and progressively increased in relative abundance (Figures 6D–6F). This was further reflected

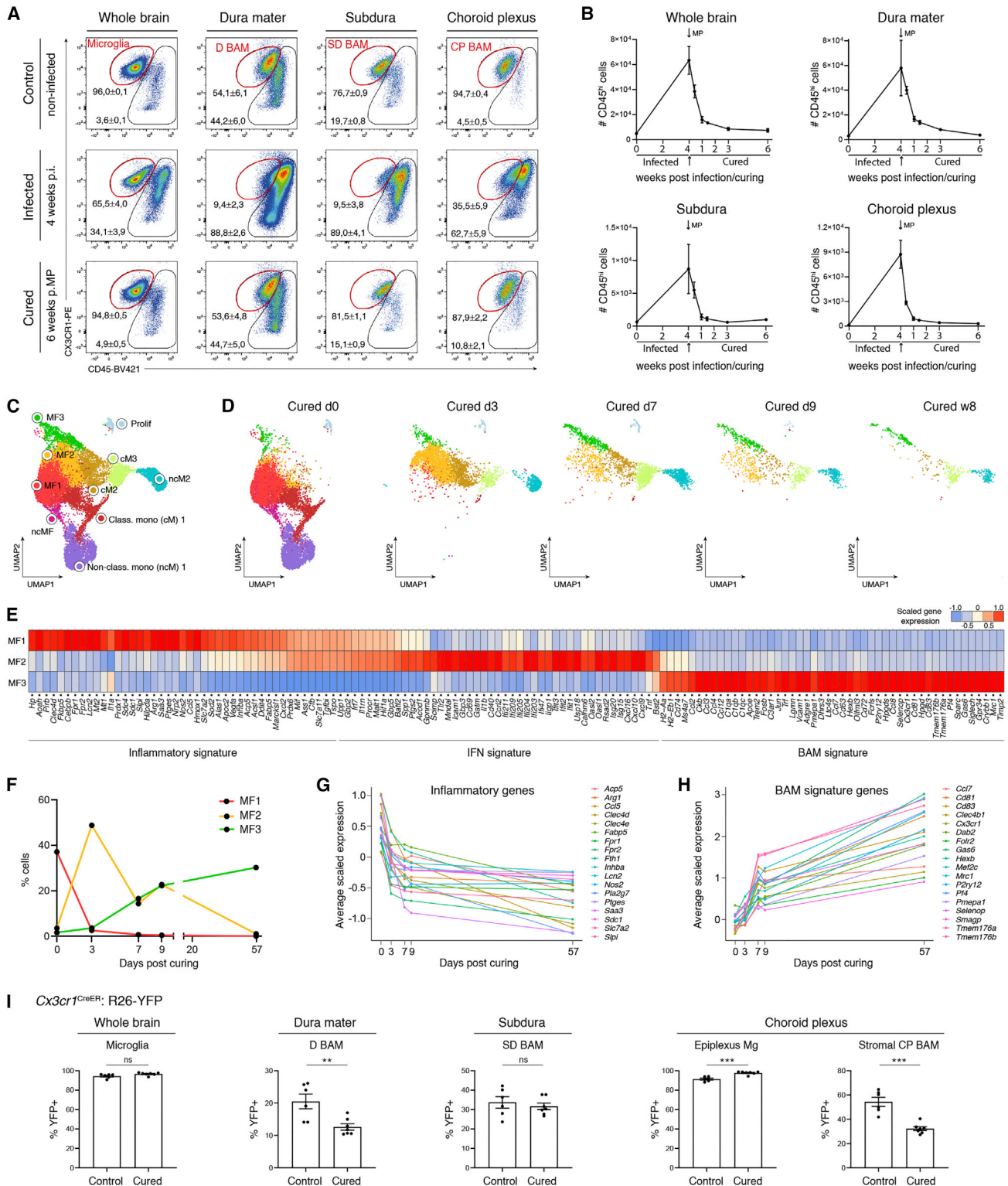


Figure 6. Recruited macrophages are short-lived cells that do not engraft as resident macrophages upon drug-induced parasite clearance (A) Flow cytometry on brain myeloid cells (pre-gated as live single CD45⁺CD11b⁺) of naive, infected, and cured mice. n = 8–10 mice/time point from 2 independent experiments.

(B) Blood-recruited myeloid cell kinetics. Mean ± SEM of n = 4–5 mice/time point, representing 2 independent experiments.

(C and D) ScRNA-seq UMAP with cluster annotation of 17,362 monocytes and macrophages (excluding microglia) from infected (d0) and cured C57BL/6J mice (C) and cluster distribution over time (D). n = 2–3 mice/time point.

(legend continued on next page)

in the global macrophage gene expression patterns, which revealed a gradual decrease of inflammatory genes, coupled to an increase of BAM signature genes (Figures 6G and 6H). This confirms that blood-recruited inflammatory macrophages are removed from the brain upon resolution of infection, and resident BAMs regain their relative abundance. We also observed new clusters of non-classical (ncM2) and classical monocytes (cM3) that infiltrated the brain from d3 post treatment and persisted over time (Figure 6D). These cells exhibited a low expression of infection-induced inflammatory genes (Figures S6F and S6G), possibly representing a new wave of postinfection monocytes.

Despite the apparent clearance of recruited macrophages, we cannot exclude that some of these cells were actually converting and engrafting as resident macrophages. To address this, we relied on fate mapping in *Cx3cr1^{CreER}:R26-YFP* mice. If recruited macrophages engraft upon disease resolution, they would be distinguishable from the pre-existing resident macrophages based on YFP expression. The total number of microglia and BAMs were not significantly different between control and cured mice (Figure S6H). Furthermore, we observed no decrease in the percentage of YFP labeling in whole brain parenchymal microglia, subdural BAMs, and epilexus microglia in cured mice as compared with control littermates (Figures 6I and S6I). This shows that upon disease resolution, there was no engraftment of recruited YFP⁺ macrophages in the brain parenchyma, subdural meninges, and apical surface of the CP epithelium. For dural and stromal CP BAMs, we did observe a significant decrease in the percentage of YFP labeling in cured versus control mice (Figure 6I). However, as these populations already exhibit continuous monocyte replacement during normal homeostasis (Goldmann et al., 2016; Van Hove et al., 2019), this suggests that BAM-turnover in the dura and CP is merely accelerated as a result of the infection.

Activated microglia progressively revert toward a homeostatic state following disease resolution, while BAMs exhibit lasting proteogenomic changes

Next, we assessed microglial transcriptional dynamics following disease resolution. Upon melarsoprol treatment, microglia clusters dynamically changed over time (Figures 7A and 7B), suggesting a continuous remodeling of gene expression. Inflammatory genes were quickly downregulated and most reached their baseline at d7–9 post curing (Figures 7C and 7D), although expression of MHCII-related genes persisted longer (Figures 7C and S7A). At d3 there was a strong but transitory spike in interferon-induced genes (Figures 7C, 7D, and S7A), possibly in response to drug-induced parasite death. We observed a gradual induction of stress related genes (e.g., *Hspa1a*, *Rad51b*, and *Dnajb1*), which peaked at d9 and was lost again by d57. Microglial signature genes increased over time, reaching high levels by d57, when microglia seemed to have readopted a homeostatic phenotype (Figures 7C, 7D, and S7A). Microglia proliferation peaked at d3 (8.8%) and dropped

to 1% by d7 and 0.09% by d57 post treatment (Figure 7E). Proliferating and non-proliferating microglia exhibited a similar activation state (Figure 7F), showing that microglia proliferation was not linked to a non-activated/homeostatic subset. Together, our results indicate that microglia undergo a stepwise deactivation, coupled to an early spike in proliferation, possibly to compensate for terminally activated cells.

To assess whether microglia and BAMs exhibited long-term transcriptional changes following infection and curing, we performed scRNA-seq on the dorsal cortex and CP of cured mice and uninfected control littermates. At 9 weeks post melarsoprol treatment, parenchymal microglia from cured mice exhibited an upregulation of MHCII-related genes as compared with controls (Figure 7G). A similar observation was made for epilexus microglia (Figure 7H). Using flow cytometry, we verified the long-term persistence of MHCII expression at the protein level. For parenchymal microglia we observed a slightly higher percentage of MHCII⁺ cells (Figures S7B and S7C). However, this was much more pronounced for epilexus microglia, where nearly half of the cells continued to express high levels of MHCII. A persistent increase in MHCII expression was also observed for dural and subdural BAMs. No significant difference was observed for stromal CP BAMs, where the majority already expressed MHCII at steady state (Figures S7B and S7C). However, when comparing gene expression in stromal CP BAMs from cured and control animals, we found that many inflammatory genes (e.g., *Cxcl9*, *Fabp5*, *C3*, and *Ccl5*) remained differentially upregulated at 9 weeks post curing (Figure 7I). Together, this suggests that microglia readopt a transcriptional profile that is very similar to the pre-infection steady state, while CP BAMs exhibit a lingering inflammatory signature that suggests a long-term remodeling of their proteogenomic state.

DISCUSSION

Seminal studies have revealed how resident macrophages play a key role in regulating tissue homeostasis. In the steady-state brain, microglia are intimately involved in synapse pruning and the removal of waste products, including protein aggregates and degenerated myelin (Prinz et al., 2019). While the functions of BAMs during steady-state conditions are still being defined, they are likely to be involved in regulating brain vasculature, CSF production and antigen presentation (Kierdorf et al., 2019). Molecular profiling uncovered the striking transcriptional diversity of resident macrophages (Gautier et al., 2012), which reflects their ability to adapt to the tissue microenvironment. This further contributed to the notion of macrophage plasticity. As resident macrophages such as microglia can efficiently self-renew and expand in numbers and these cells are professed to be highly plastic, then why is there a need to recruit monocytes to the brain during certain pathologies? Our results indicate that during brain infection with *T. brucei*, monocytes are recruited to the brain in large numbers. Single-cell analysis revealed that

(E) Heatmap highlighting gene signatures of macrophages (MF1–3).

(F–H) Macrophage kinetics (F) and gene expression dynamics over time (G and H).

(I) Fate mapping in cured (9w) and control *Cx3cr1^{CreER}:R26-YFP* mice. Epilexus Mg were gated as shown in Figure S6I. Mean ± SEM. of n = 6–7 mice/group, representing 3 independent experiments. Significance evaluated by unpaired t tests, ns, **p < 0.01, ***p < 0.001. Statistics, Table S3. See also Figure S6.

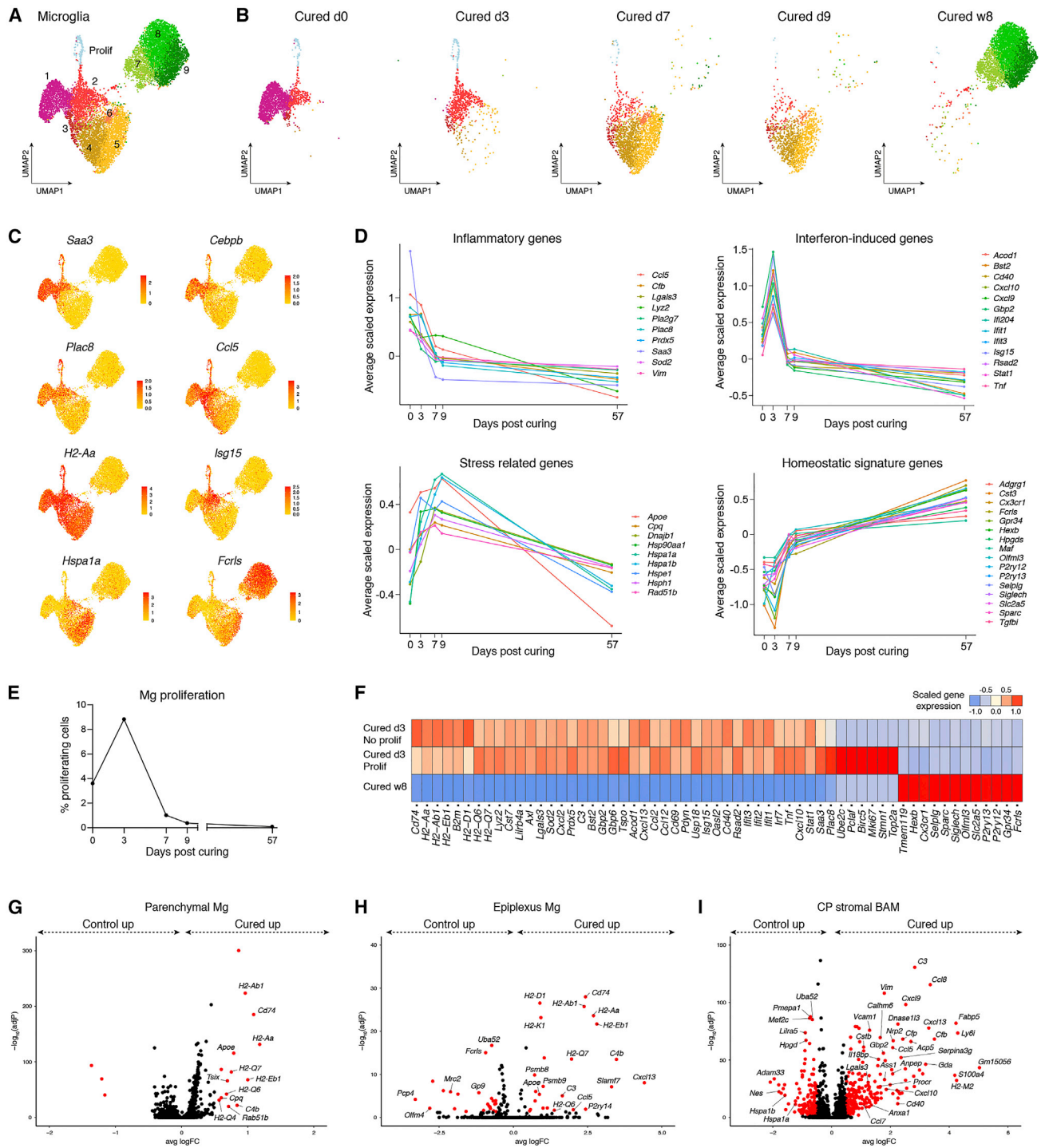


Figure 7. Microglia progressively revert toward homeostasis, while BAMS show lasting transcriptional changes

(A and B) ScRNA-seq UMAP with cluster annotation of 10,660 microglia from infected (d0) and cured C57BL/6J mice (A) and cluster distribution over time (B). n = 2–3 mice/time point.

(C and D) Expression levels (C) and temporal dynamics (D) of genes associated with activation/inflammation, stress response, and homeostasis.

(E) Microglia proliferation over time.

(F) Heatmap highlighting transcriptional similarity of proliferating and non-proliferating cells at d3.

(G–I) VP showing DE genes (red, adj p < 0.05, abs(log₂FC) > 0.5) in cortical microglia (G), epileptus Mg (H), and CP stromal BAMS (I) of cured (9w) versus control Cx3cr1^{CreER}:R26-YFP mice. n = 8 control (pooled) and 6 cured (pooled) mice.

recruited monocyte-derived macrophages adopted transcriptional states that were distinct from those of resident microglia or BAMs, indicating that monocytes react differently to the ongoing tissue inflammation. This may in part result from the differential expression of certain immune receptors in monocytes. Alternatively, as resident macrophages are programmed to perform important homeostatic functions, they may have epigenetic modifications that restrict their plasticity (Lavin et al., 2014). This is in agreement with transplantation studies, where transplanted monocytes can develop into resident alveolar macrophages, while transplanted peritoneal macrophages do not (van de Laar et al., 2016; Lavin et al., 2014). Furthermore, since the first discovery of the DAM phenotype in amyloid models of Alzheimer's disease (Keren-Shaul et al., 2017), highly similar microglial activation states have been observed in many other pathological conditions, but also in settings unrelated to disease (Anderson et al., 2019; Hammond et al., 2019; Jordão et al., 2019; Li et al., 2019; Masuda et al., 2019; Safaiyan et al., 2021; Van Hove et al., 2019). This includes proliferative-region-associated microglia found in the developing brain, microglia associated to white matter tracts, or microglia on the apical surface of CP epithelium. While some transcriptional variations may be observed between these populations, they share the same core activation signature. This is confirmed in our current study, showing that while DAM genes are once again observed, microglia show a much lower expression of many of the antimicrobial or inflammatory genes that are induced in recruited macrophages. Recruitment of monocytes during brain inflammation may thus allow for the establishment of macrophage populations that have complementary functions or are better adapted to deal with the ongoing insult. This is likely not restricted to the brain, as resident and recruited macrophages also react differently to nematode infections in the peritoneum (Rückerl et al., 2017). Recruited brain macrophages may also be detrimental, for example, in the context of autoimmune neuroinflammation (Ajami et al., 2011; Yamasaki et al., 2014). While during *T. brucei* infection, microglia and BAMs were found to promote brain barrier permeability and the recruitment of monocytes, during acute demyelination, microglia limit the dispersion of recruited macrophages (Plemel et al., 2020). This indicates that the disease context determines the interplay between resident and recruited macrophages.

In infected brains, microglia exhibited a profound accumulation around periventricular regions. Furthermore, we observed a significant expansion of epiplexus cells, which were derived from *Sall1*⁺ cells and transcriptionally resembled microglia. Since epiplexus microglia are also observed in homeostatic brains (Van Hove et al., 2019), their increase during infection may result from local expansion. However, as microglia accumulated near the ependyma, epiplexus microglia may also partly be derived from parenchymal microglia that infiltrate from the periventricular tissue. This would highlight the remarkable motility of microglia, showing that they can migrate from one brain compartment to another. Recent *in vivo* imaging studies showed that epiplexus cells are highly mobile and can travel over large distances on the CP epithelium (Shiple et al., 2020). However, new fate mapping approaches are needed to confirm whether epiplexus cells indeed derive from neighboring parenchymal microglia.

Fate mapping studies have revealed that in many adult tissues, macrophages have an embryonic origin and self-renew *in situ* (Ginhoux and Guilliams, 2016). In the brain of healthy mice, microglia and certain BAM populations remain to be yolk sac derived throughout life. Still, bone marrow (BM)-derived microglia do develop under specific experimental conditions, for example, following irradiation and BM reconstitution (Shemer et al., 2018) or upon genetic depletion of embryonic microglia (Bennett et al., 2018; Cronk et al., 2018; Lund et al., 2018). As these are quite artificial conditions, it remains unclear whether BM engraftment in the brain occurs following more naturally occurring insults. For example, does monocyte recruitment during CNS infections open the door to their engraftment as resident cells upon disease resolution? We show that upon drug-mediated resolution of *T. brucei* infection, recruited brain macrophages quickly disappeared and no BM-derived microglia were detected in cured mice. In the border regions, we observed increased BM engraftment in the blood-accessible dura and stromal CP, but not in the subdural meninges. Rua et al. (2019) have also shown increased BM engraftment in the dura following recovery from meningitis. We propose a model in which monocyte-derived macrophages that are recruited during infection develop into short-lived cells that are removed from all brain compartments upon disease resolution. As brain barrier integrity was rapidly restored, we suggest that the brain parenchyma and subdural meninges become inaccessible to peripheral monocytes shortly after parasite elimination. However, in the dura and CP stroma, monocytes continue to be recruited and those that enter when inflammation has subsided are able to engraft as resident BAMs. During experimental autoimmune encephalitis, recruited monocyte-derived cells that accumulate around the spinal cord leptomeninges also do not engraft as microglia following disease remission (Ajami et al., 2011). However, in peripheral organs such as the lung, liver, and peritoneum, monocytes can contribute to the resident macrophage pool upon disease resolution (Aegerter et al., 2020; Louwe et al., 2021; Machiels et al., 2017; Remmerie et al., 2020; Tran et al., 2020). An explanation for the discrepancy between the brain and these peripheral organs may be the presence of the blood-brain barrier, which can block monocyte infiltration when inflammation subsides. Furthermore, infection and disease often result in the death of resident macrophages in peripheral tissues (Jenkins and Allen, 2021). This so-called “macrophage disappearance reaction” may be a feature of intracellular pathogens as it was not observed during *T. brucei* infections. Thus, the persistence of resident brain macrophages may prevent recruited monocytes to engraft in the macrophage niche.

How does the resident brain macrophage pool return to homeostasis following disease resolution? As DAMs may undergo replicative senescence (Hu et al., 2021), one possibility is that the majority of activated microglia would die and be replaced by the clonal expansion of non-activated homeostatic microglia. During experimental demyelination, pro-inflammatory microglia also undergo necroptosis followed by repopulation (Lloyd et al., 2019). Yet, our scRNA-seq kinetic indicated that upon *T. brucei* disease resolution, the bulk of microglia underwent a stepwise deactivation and readopted a homeostatic phenotype within 8 weeks. CP BAMs of cured animals did exhibit a lingering inflammatory signature. These alterations may reflect cell

intrinsic adaptations, such as epigenetic reprogramming, indicative of innate memory or trained immunity (Netea et al., 2011). Alternatively, it may result from changes in the tissue niche, especially in the border regions that underwent severe inflammation. The transcriptional or epigenetic changes in resident brain macrophages may alter their response to future insults (Rua et al., 2019; Wendeln et al., 2018). Understanding how these alterations affect homeostasis and disease requires further investigation.

Limitations of the study

Our findings on the dynamics of brain-resident and recruited macrophages in *Trypanosoma brucei* infected mice may not be generalizable to all types of brain infections. The host response may depend on the type of pathogen, encompassing phylogenetically diverse bacterial, viral, and eukaryote species, as well as on the nature of the pathogen's life cycle and whether it lives intra- or extracellularly. Due to the current lack of appropriate genetic tools, we were unable to evaluate the functional role of individual subsets of resident macrophages, such as microglia versus BAMs, or parenchymal versus epiplexus microglia. This remains an important future perspective once new tools are developed.

STAR★METHODS

Detailed methods are provided in the online version of this paper and include the following:

- KEY RESOURCES TABLE
- RESOURCE AVAILABILITY
 - Lead contact
 - Materials availability
 - Data and code availability
- EXPERIMENTAL MODEL AND SUBJECT DETAILS
 - Mice
 - Parasites
- METHOD DETAILS
 - Tamoxifen treatment
 - Parasite infection
 - Diphtheria toxin treatment
 - Melarsoprol treatment
 - Blood and CSF isolation
 - Single cell isolation from brain (regions)
 - Parasitemia counts
 - Immunohistochemistry
 - Morphology quantification of BAMs
 - Serial 2-photon tomography
 - Assessment of brain barrier leakage
 - Cytokine measurements in CSF
 - Flow cytometry and cell sorting
 - Assessment of apoptosis via flow cytometry
 - ScRNA-seq using 10x Genomics platform
 - Gene expression data processing
 - Heatmaps, GO enrichment and triwise plots
 - x,y-representation of gene expression dynamics
 - Schematic representations using Biorender
 - Experimental design
- QUANTIFICATION AND STATISTICAL ANALYSIS

SUPPLEMENTAL INFORMATION

Supplemental information can be found online at <https://doi.org/10.1016/j.immuni.2022.09.005>.

ACKNOWLEDGMENTS

This work was supported by an Innoviris grant (Attract grant BB2B 2015-2), a Collen-Franqui start-up grant, and a grant by Wetenschappelijk Fonds Willy Gepts of the UZ Brussel to K.M. and K.D.V. We thank Y. Elkrim, J. Van De Vaerd, E. Himpe, G. Van Imschoot, N. Gorié, the VIB Flow Core, the VIB Nucleomics Core, and the VIB BioImaging Core for technical assistance; VIB Tech Watch and Martin Williams' lab for support regarding scRNA-seq technologies; Tissue Vision Inc. for the acquisition and mapping of serial two-photon tomography data; J.R. Franco Minguell and G. Priotto of the World Health Organization and Sanofi for providing Melarsoprol; C. De Trez for discussions; and S. Blotwijk for advice on statistical analysis.

AUTHOR CONTRIBUTIONS

K.M. and K.D.V. conceived the study and designed experiments. K.D.V., H.V.H., I.S., A.R.P.A., J.B., M.V.-P., L.A., M.M., L.D., J.F.M., R.C., G.C., B.S., R.E.V., and K.M. performed experiments. K.D.V., J.B., L.D., D.D.B., and A.M. carried out data analyses. K.D.V., D.K., and K.M. performed or helped with bioinformatics analyses. L.B., D.D.B., A.M., J.A.V.G., and R.E.V. provided advice on experimental design, data analyses, and interpretation. K.D.V. and K.M. wrote the manuscript. K.M. directed the study.

DECLARATION OF INTERESTS

The authors declare no competing interests.

Received: December 8, 2021

Revised: July 11, 2022

Accepted: September 7, 2022

Published: October 12, 2022

REFERENCES

- Aegerter, H., Kulikauskaite, J., Crotta, S., Patel, H., Kelly, G., Hessel, E.M., Mack, M., Beinke, S., and Wack, A. (2020). Influenza-induced monocyte-derived alveolar macrophages confer prolonged antibacterial protection. *Nat. Immunol.* 21, 145–157. <https://doi.org/10.1038/s41590-019-0568-x>.
- Ajami, B., Bennett, J.L., Krieger, C., McNagny, K.M., and Rossi, F.M.V. (2011). Infiltrating monocytes trigger EAE progression, but do not contribute to the resident microglia pool. *Nat. Neurosci.* 14, 1142–1149. <https://doi.org/10.1038/nn.2887>.
- Anderson, S.R., Roberts, J.M., Zhang, J., Steele, M.R., Romero, C.O., Bosco, A., and Vetter, M.L. (2019). Developmental apoptosis promotes a disease-related gene signature and independence from CSF1R signaling in retinal microglia. *Cell Rep.* 27, 2002–2013.e5. <https://doi.org/10.1016/j.celrep.2019.04.062>.
- Arganda-Carreras, I., Fernández-González, R., Muñoz-Barrutia, A., and Ortiz-de-Solorzano, C. (2010). 3D reconstruction of histological sections: application to mammary gland tissue. *Microsc. Res. Tech.* 73, 1019–1029. <https://doi.org/10.1002/jemt.20829>.
- Bennett, F.C., Bennett, M.L., Yaqoob, F., Mulinyawe, S.B., Grant, G.A., Hayden Gephart, M., Plowey, E.D., and Barres, B.A. (2018). A combination of ontogeny and CNS environment establishes microglial identity. *Neuron* 98, 1170–1183.e8. <https://doi.org/10.1016/j.neuron.2018.05.014>.
- Benz, C., Martins, V.C., Radtke, F., and Bleul, C.C. (2008). The stream of precursors that colonizes the thymus proceeds selectively through the early T lineage precursor stage of T cell development. *J. Exp. Med.* 205, 1187–1199. <https://doi.org/10.1084/jem.20072168>.
- Bruttger, J., Karram, K., Wörtge, S., Regen, T., Marini, F., Hoppmann, N., Klein, M., Blank, T., Yona, S., Wolf, Y., et al. (2015). Genetic Cell Ablation Reveals

Clusters of Local Self-Renewing Microglia in the Mammalian Central Nervous System. *Immunity* 43.

- Buch, T., Heppner, F.L., Tertilt, C., Heinen, T.J.A.J., Kremer, M., Wunderlich, F.T., Jung, S., and Waisman, A. (2005). A cre-inducible diphtheria toxin receptor mediates cell lineage ablation after toxin administration. *Nat. Methods* 2, 419–426. <https://doi.org/10.1038/nmeth762>.
- Burrell-Saward, H., Rodgers, J., Bradley, B., Croft, S.L., and Ward, T.H. (2015). A sensitive and reproducible in vivo imaging mouse model for evaluation of drugs against late-stage human African trypanosomiasis. *J. Antimicrob. Chemother.* 70, 510–517. <https://doi.org/10.1093/jac/dku393>.
- Butovsky, O., Jedrychowski, M.P., Moore, C.S., Cialic, R., Lanser, A.J., Gabriely, G., Koeglsperger, T., Dake, B., Wu, P.M., Doykan, C.E., et al. (2014). Identification of a unique TGF- β -dependent molecular and functional signature in microglia. *Nat. Neurosci.* 17, 131–143. <https://doi.org/10.1038/nn.3599>.
- Caljon, G., Van Reet, N., De Trez, C., Vermeersch, M., Pérez-Morga, D., and Van Den Abbeele, J. (2016). The dermis as a delivery site of *Trypanosoma brucei* for Tsetse flies. *PLoS Pathog.* 12, e1005744. <https://doi.org/10.1371/journal.ppat.1005744>.
- Cronk, J.C., Filiano, A.J., Louveau, A., Marin, I., Marsh, R., Ji, E., Goldman, D.H., Smirnov, I., Geraci, N., Acton, S., et al. (2018). Peripherally derived macrophages can engraft the brain independent of irradiation and maintain an identity distinct from microglia. *J. Exp. Med.* 215, 1627–1647. <https://doi.org/10.1084/jem.20180247>.
- Engelhardt, B., Wolburg-Buchholz, K., and Wolburg, H. (2001). Involvement of the choroid plexus in central nervous system inflammation. *Microsc. Res. Tech.* 52, 112–129. [https://doi.org/10.1002/1097-0029\(20010101\)52:1<112::AID-JEMT13>3.0.CO;2-5](https://doi.org/10.1002/1097-0029(20010101)52:1<112::AID-JEMT13>3.0.CO;2-5).
- Faul, F., Erdfelder, E., Lang, A.G., and Buchner, A. (2007). G*Power 3: a flexible statistical power analysis program for the social, behavioral, and biomedical sciences. *Behav. Res. Methods* 39, 175–191. <https://doi.org/10.3758/bf03193146>.
- Faust, N., Varas, F., Kelly, L.M., Heck, S., and Graf, T. (2000). Insertion of enhanced green fluorescent protein into the lysozyme gene creates mice with green fluorescent granulocytes and macrophages. *Blood* 96, 719–726.
- Gautier, E.L., Shay, T., Miller, J., Greter, M., Jakubzick, C., Ivanov, S., Helft, J., Chow, A., Elpek, K.G., Gordonov, S., et al. (2012). Gene-expression profiles and transcriptional regulatory pathways that underlie the identity and diversity of mouse tissue macrophages. *Nat. Immunol.* 13, 1118–1128. <https://doi.org/10.1038/ni.2419>.
- Ginhoux, F., Greter, M., Leboeuf, M., Nandi, S., See, P., Gokhan, S., Mehler, M.F., Conway, S.J., Ng, L.G., Stanley, E.R., et al. (2010). Fate mapping analysis reveals that adult microglia derive from primitive macrophages. *Science* 330, 841–845. <https://doi.org/10.1126/science.1194637>.
- Ginhoux, F., and Williams, M. (2016). Tissue-resident macrophage ontogeny and homeostasis. *Immunity* 44, 439–449. <https://doi.org/10.1016/j.immuni.2016.02.024>.
- Goldmann, T., Wieghofer, P., Jordão, M.J.C., Prutek, F., Hagemeyer, N., Frenzel, K., Amann, L., Staszewski, O., Kierdorf, K., Krueger, M., et al. (2016). Origin, fate and dynamics of macrophages at central nervous system interfaces. *Nat. Immunol.* 17, 797–805. <https://doi.org/10.1038/ni.3423>.
- Goldmann, T., Wieghofer, P., Müller, P.F., Wolf, Y., Varol, D., Yona, S., Brendecke, S.M., Kierdorf, K., Staszewski, O., Datta, M., et al. (2013). A new type of microglia gene targeting shows TAK1 to be pivotal in CNS autoimmune inflammation. *Nat. Neurosci.* 16, 1618–1626. <https://doi.org/10.1038/nn.3531>.
- Haase, R., Royer, L.A., Steinbach, P., Schmidt, D., Dibrov, A., Schmidt, U., Weigert, M., Maghelli, N., Tomancak, P., Jug, F., and Myers, E.W. (2020). CLUJ: GPU-accelerated image processing for everyone. *Nat. Methods* 17, 5–6. <https://doi.org/10.1038/s41592-019-0650-1>.
- Hammond, T.R., Dufort, C., Dissing-Olesen, L., Giera, S., Young, A., Wysoker, A., Walker, A.J., Gergits, F., Segel, M., Nemes, J., et al. (2019). Single-cell RNA sequencing of microglia throughout the mouse lifespan and in the injured brain reveals complex cell-state changes. *Immunity* 50, 253–271.e6. <https://doi.org/10.1016/j.immuni.2018.11.004>.
- Hickman, S.E., Kingery, N.D., Ohsumi, T.K., Borowsky, M.L., Wang, L.-C., Means, T.K., and El Khoury, J. (2013). The microglial sensome revealed by direct RNA sequencing. *Nat. Neurosci.* 16, 1896–1905. <https://doi.org/10.1038/nn.3554>.
- Hu, Y., Fryatt, G.L., Ghorbani, M., Obst, J., Menassa, D.A., Martin-Estebane, M., Muntslag, T.A.O., Olmos-Alonso, A., Guerrero-Carrasco, M., Thomas, D., et al. (2021). Replicative senescence dictates the emergence of disease-associated microglia and contributes to A β pathology. *Cell Rep.* 35, 109228. <https://doi.org/10.1016/j.celrep.2021.109228>.
- Inoue, S., Inoue, M., Fujimura, S., and Nishinakamura, R. (2010). A mouse line expressing Sall1-driven inducible cre recombinase in the kidney mesenchyme. *Genesis* 48, 207–212. <https://doi.org/10.1002/dvg.20603>.
- Jenkins, S.J., and Allen, J.E. (2021). The expanding world of tissue-resident macrophages. *Eur. J. Immunol.* 51, 1882–1896. <https://doi.org/10.1002/eji.202048881>.
- Jordão, M.J.C., Sankowski, R., Brendecke, S.M., Sagar, Locatelli, G., Tai, Y.H., Tay, T.L., Schramm, E., Armbruster, S., Hagemeyer, N., et al. (2019). Single-cell profiling identifies myeloid cell subsets with distinct fates during neuroinflammation. *Science* 363, eaat7554. <https://doi.org/10.1126/science.aat7554>.
- Jung, S., Aliberti, J., Graemmel, P., Sunshine, M.J., Kreutzberg, G.W., Sher, A., and Littman, D.R. (2000). Analysis of fractalkine receptor CX3CR1 function by targeted deletion and green fluorescent protein reporter gene insertion. *Mol. Cell. Biol.* 20, 4106–4114. <https://doi.org/10.1128/MCB.20.11.4106-4114.2000>.
- Kennedy, P.G.E., and Rodgers, J. (2019). Clinical and neuropathogenetic aspects of human African trypanosomiasis. *Front. Immunol.* 10, 39. <https://doi.org/10.3389/fimmu.2019.00039>.
- Keren-Shaul, H., Spinrad, A., Weiner, A., Matcovitch-Natan, O., Dvir-Szternfeld, R., Ulland, T.K., David, E., Baruch, K., Lara-Astaiso, D., Toth, B., et al. (2017). A unique microglia type associated with restricting development of Alzheimer’s disease. *Cell* 169, 1276–1290.e17. <https://doi.org/10.1016/j.cell.2017.05.018>.
- Kierdorf, K., Masuda, T., Jordão, M.J.C., and Prinz, M. (2019). Macrophages at CNS interfaces: ontogeny and function in health and disease. *Nat. Rev. Neurosci.* 20, 547–562. <https://doi.org/10.1038/s41583-019-0201-x>.
- Korsunsky, I., Millard, N., Fan, J., Slowikowski, K., Zhang, F., Wei, K., Baglaenko, Y., Brenner, M., Loh, P.-R., and Raychaudhuri, S. (2019). Fast, sensitive and accurate integration of single-cell data with Harmony. *Nat. Methods* 16, 1289–1296. <https://doi.org/10.1038/s41592-019-0619-0>.
- Kristensson, K., Nygård, M., Bertini, G., and Bentivoglio, M. (2010). African trypanosome infections of the nervous system: parasite entry and effects on sleep and synaptic functions. *Prog. Neurobiol.* 91, 152–171. <https://doi.org/10.1016/j.pneurobio.2009.12.001>.
- Lavin, Y., Winter, D., Blecher-Gonen, R., David, E., Keren-Shaul, H., Merad, M., Jung, S., and Amit, I. (2014). Tissue-resident macrophage enhancer landscapes are shaped by the local microenvironment. *Cell* 159, 1312–1326. <https://doi.org/10.1016/j.cell.2014.11.018>.
- Lee, T.-C., Kashyap, R.L., and Chu, C.N. (1994). Building skeleton models via 3-D medial surface/axis thinning algorithms. *CVGIP Graph. Models. Image Process.* 56, 462–478. <https://doi.org/10.1006/cgip.1994.1042>.
- Legland, D., Arganda-Carreras, I., and Andrey, P. (2016). MorphoLibJ: integrated library and plugins for mathematical morphology with ImageJ. *Bioinformatics* 32, 3532–3534. <https://doi.org/10.1093/bioinformatics/btw413>.
- Li, Q., Cheng, Z., Zhou, L., Darmanis, S., Neff, N.F., Okamoto, J., Gulati, G., Bennett, M.L., Sun, L.O., Clarke, L.E., et al. (2019). Developmental heterogeneity of microglia and brain myeloid cells revealed by deep single-cell RNA sequencing. *Neuron* 101, 207–223.e10. <https://doi.org/10.1016/j.neuron.2018.12.006>.
- Lloyd, A.F., Davies, C.L., Holloway, R.K., Labrak, Y., Ireland, G., Carradori, D., Dillenburg, A., Borger, E., Soong, D., Richardson, J.C., et al. (2019). Central nervous system regeneration is driven by microglia necroptosis and repopulation. *Nat. Neurosci.* 22, 1046–1052. <https://doi.org/10.1038/s41593-019-0418-z>.

- Louveau, A., Smirnov, I., Keyes, T.J., Eccles, J.D., Rouhani, S.J., Peske, J.D., Derecki, N.C., Castle, D., Mandell, J.W., Lee, K.S., et al. (2015). Structural and functional features of central nervous system lymphatic vessels. *Nature* 523, 337–341. <https://doi.org/10.1038/nature14432>.
- Louwe, P.A., Badiola Gomez, L., Webster, H., Perona-Wright, G., Bain, C.C., Forbes, S.J., and Jenkins, S.J. (2021). Recruited macrophages that colonize the post-inflammatory peritoneal niche convert into functionally divergent resident cells. *Nat. Commun.* 12, 1770. <https://doi.org/10.1038/s41467-021-21778-0>.
- Lun, A.T.L., McCarthy, D.J., and Marioni, J.C. (2016). A step-by-step workflow for low-level analysis of single-cell RNA-seq data with Bioconductor. *F1000Res* 5, 2122. <https://doi.org/10.12688/f1000research.9501.2>.
- Lun, A.T.L., Riesenfeld, S., Andrews, T., Dao, T.P., Gomes, T., and Marioni, J.C. (2019). EmptyDrops: distinguishing cells from empty droplets in droplet-based single-cell RNA sequencing data. *Genome Biol.* 20, 63. <https://doi.org/10.1186/s13059-019-1662-y>.
- Lund, H., Pieber, M., Parsa, R., Han, J., Grommisch, D., Ewing, E., Kular, L., Needhamsen, M., Espinosa, A., Nilsson, E., et al. (2018). Competitive repopulation of an empty microglial niche yields functionally distinct subsets of microglia-like cells. *Nat. Commun.* 9, 4845. <https://doi.org/10.1038/s41467-018-07295-7>.
- Machiels, B., Dourcy, M., Xiao, X., Javaux, J., Mesnil, C., Sabatel, C., Desmecht, D., Lallemand, F., Martinive, P., Hammad, H., et al. (2017). A gammaherpesvirus provides protection against allergic asthma by inducing the replacement of resident alveolar macrophages with regulatory monocytes. *Nat. Immunol.* 18, 1310–1320. <https://doi.org/10.1038/ni.3857>.
- Magez, S., and Caljon, G. (2011). Mouse models for pathogenic African trypanosomes: unravelling the immunology of host-parasite-vector interactions. *Parasite Immunol.* 33, 423–429. <https://doi.org/10.1111/j.1365-3024.2011.01293.x>.
- Mastorakos, P., and McGavern, D. (2019). The anatomy and immunology of vasculature in the central nervous system. *Sci. Immunol.* 4, eaav0492. <https://doi.org/10.1126/sciimmunol.aav0492>.
- Masuda, T., Sankowski, R., Staszewski, O., Böttcher, C., Amann, L., Sagar, Scheiwe, C., Nessler, S., Kunz, P., van Loo, G., et al. (2019). Spatial and temporal heterogeneity of mouse and human microglia at single-cell resolution. *Nature* 566, 388–392. <https://doi.org/10.1038/s41586-019-0924-x>.
- McCarthy, D.J., Campbell, K.R., Lun, A.T.L., and Wills, Q.F. (2017). Scater: pre-processing, quality control, normalization and visualization of single-cell RNA-seq data in R. *Bioinformatics* 33, 1179–1186. <https://doi.org/10.1093/bioinformatics/btw777>.
- Mrdjen, D., Pavlovic, A., Hartmann, F.J., Schreiner, B., Utz, S.G., Leung, B.P., Lelios, I., Heppner, F.L., Kipnis, J., Merkler, D., et al. (2018). High-dimensional single-cell mapping of central nervous system immune cells reveals distinct myeloid subsets in health, aging, and disease. *Immunity* 48, 380–395.e6. <https://doi.org/10.1016/j.immuni.2018.01.011>.
- Netea, M.G., Quintin, J., and van der Meer, J.W.M. (2011). Trained immunity: a memory for innate host defense. *Cell Host Microbe* 9, 355–361. <https://doi.org/10.1016/j.chom.2011.04.006>.
- Obal, F., and Krueger, J.M. (2004). GHRH and sleep. *Sleep Med. Rev.* 8, 367–377. <https://doi.org/10.1016/j.smrv.2004.03.005>.
- Plemel, J.R., Stratton, J.A., Michaels, N.J., Rawji, K.S., Zhang, E., Sinha, S., Baaklini, C.S., Dong, Y., Ho, M., Thorburn, K., et al. (2020). Microglia response following acute demyelination is heterogeneous and limits infiltrating macrophage dispersion. *Sci. Adv.* 6, eaay6324. <https://doi.org/10.1126/sciadv.aay6324>.
- Pombo Antunes, A.R., Scheyltjens, I., Lodi, F., Messiaen, J., Antoranz, A., Duerinck, J., Kancheva, D., Martens, L., De Vlamincck, K., Van Hove, H., et al. (2021). Single-cell profiling of myeloid cells in glioblastoma across species and disease stage reveals macrophage competition and specialization. *Nat. Neurosci.* 24, 595–610. <https://doi.org/10.1038/s41593-020-00789-y>.
- Prinz, M., Jung, S., and Priller, J. (2019). Microglia biology: one century of evolving concepts. *Cell* 179, 292–311. <https://doi.org/10.1016/j.cell.2019.08.053>.
- Ragan, T., Kadiri, L.R., Venkataraju, K.U., Bahlmann, K., Sutin, J., Taranda, J., Arganda-Carreras, I., Kim, Y., Seung, H.S., and Osten, P. (2012). Serial two-photon tomography for automated ex vivo mouse brain imaging. *Nat. Methods* 9, 255–258. <https://doi.org/10.1038/nmeth.1854>.
- Remmerie, A., Martens, L., Thoné, T., Castoldi, A., Seurinck, R., Pavie, B., Roels, J., Vanneste, B., De Prijck, S., Vanhockerhout, M., et al. (2020). Osteopontin expression identifies a subset of recruited macrophages distinct from Kupffer cells in the fatty liver. *Immunity* 53, 641–657.e14. <https://doi.org/10.1016/j.immuni.2020.08.004>.
- Rua, R., Lee, J.Y., Silva, A.B., Swafford, I.S., Maric, D., Johnson, K.R., and McGavern, D.B. (2019). Infection drives meningeal engraftment by inflammatory monocytes that impairs CNS immunity. *Nat. Immunol.* 20, 407–419. <https://doi.org/10.1038/s41590-019-0344-y>.
- Rückerl, D., Campbell, S.M., Duncan, S., Sutherland, T.E., Jenkins, S.J., Hewitson, J.P., Barr, T.A., Jackson-Jones, L.H., Maizels, R.M., and Allen, J.E. (2017). Macrophage origin limits functional plasticity in helminth-bacterial co-infection. *PLoS Pathog.* 13, e1006233. <https://doi.org/10.1371/journal.ppat.1006233>.
- Rustenhoven, J., Drieu, A., Mamuladze, T., de Lima, K.A., Dykstra, T., Wall, M., Papadopoulos, Z., Kanamori, M., Salvador, A.F., Baker, W., et al. (2021). Functional characterization of the dural sinuses as a neuroimmune interface. *Cell* 184, 1000–1016.e27. <https://doi.org/10.1016/j.cell.2020.12.040>.
- Safaiyan, S., Besson-Girard, S., Kaya, T., Cantuti-Castelvetri, L., Liu, L., Ji, H., Schifferer, M., Gouna, G., Usifo, F., Kannaiyan, N., et al. (2021). White matter aging drives microglial diversity. *Neuron* 109, 1100–1117.e10. <https://doi.org/10.1016/j.neuron.2021.01.027>.
- Saper, C.B., Scammell, T.E., and Lu, J. (2005). Hypothalamic regulation of sleep and circadian rhythms. *Nature* 437, 1257–1263. <https://doi.org/10.1038/nature04284>.
- Satija, R., Farrell, J.A., Gennert, D., Schier, A.F., and Regev, A. (2015). Spatial reconstruction of single-cell gene expression data. *Nat. Biotechnol.* 33, 495–502. <https://doi.org/10.1038/nbt.3192>.
- Scheyltjens, I., Van Hove, H., De Vlamincck, K., Kancheva, D., Bastos, J., Vara-Pérez, M., Pombo Antunes, A.R., Martens, L., Scott, C.L., Van Ginderachter, J.A., et al. (2022). Single-cell RNA and protein profiling of immune cells from the mouse brain and its border tissues. *Nat. Protoc.* <https://doi.org/10.1038/s41596-022-00716-4>.
- Schindelin, J., Arganda-Carreras, I., Frise, E., Kaynig, V., Longair, M., Pietzsch, T., Preibisch, S., Rueden, C., Saalfeld, S., Schmid, B., et al. (2012). Fiji: an open-source platform for biological-image analysis. *Nat. Methods* 9, 676–682. <https://doi.org/10.1038/nmeth.2019>.
- Shechter, R., London, A., and Schwartz, M. (2013). Orchestrated leukocyte recruitment to immune-privileged sites: absolute barriers versus educational gates. *Nat. Rev. Immunol.* 13, 206–218. <https://doi.org/10.1038/nri3391>.
- Shemer, A., Grozovski, J., Tay, T.L., Tao, J., Volaski, A., Süß, P., Ardura-Fabregat, A., Gross-Vered, M., Kim, J.S., David, E., et al. (2018). Engrafted parenchymal brain macrophages differ from microglia in transcriptome, chromatin landscape and response to challenge. *Nat. Commun.* 9, 5206. <https://doi.org/10.1038/s41467-018-07548-5>.
- Shiple, F.B., Dani, N., Xu, H., Deister, C., Cui, J., Head, J.P., Sadegh, C., Fame, R.M., Shannon, M.L., Flores, V.I., et al. (2020). Tracking calcium dynamics and immune surveillance at the choroid plexus blood-cerebrospinal fluid interface. *Neuron* 108, 623–639.e10. <https://doi.org/10.1016/j.neuron.2020.08.024>.
- Srinivas, S., Watanabe, T., Lin, C.S., William, C.M., Tanabe, Y., Jessell, T.M., and Costantini, F. (2001). Cre reporter strains produced by targeted insertion of EYFP and ECFP into the ROSA26 locus. *BMC Dev. Biol.* 1, 4. <https://doi.org/10.1186/1471-213x-1-4>.
- Steffen, B.J., Breier, G., Butcher, E.C., Schulz, M., and Engelhardt, B. (1996). ICAM-1, VCAM-1, and MAdCAM-1 are expressed on choroid plexus epithelium but not endothelium and mediate binding of lymphocytes in vitro. *Am. J. Pathol.* 148, 1819–1838.
- Sternberg, S.R. (1983). Biomedical image processing. *Computer* 16, 22–34. <https://doi.org/10.1109/MC.1983.1654163>.

- Stijlemans, B., Caljon, G., Van Den Abbeele, J., Van Ginderachter, J.A., Magez, S., and De Trez, C. (2016). Immune evasion strategies of *Trypanosoma brucei* within the mammalian host: progression to pathogenicity. *Front. Immunol.* 7, 233. <https://doi.org/10.3389/fimmu.2016.00233>.
- Stijlemans, B., Leng, L., Brys, L., Sparkes, A., Vansintjan, L., Caljon, G., Raes, G., Van Den Abbeele, J., Van Ginderachter, J.A., Beschin, A., et al. (2014). MIF contributes to *Trypanosoma brucei* associated immunopathogenicity development. *PLoS Pathog.* 10, e1004414. <https://doi.org/10.1371/journal.ppat.1004414>.
- Stuart, T., Butler, A., Hoffman, P., Hafemeister, C., Papalexi, E., Mauck, W.M., Hao, Y., Stoeckius, M., Smibert, P., and Satija, R. (2019). Comprehensive integration of single-cell data. *Cell* 177, 1888–1902.e21. <https://doi.org/10.1016/j.cell.2019.05.031>.
- Tran, S., Baba, I., Poupel, L., Dussaud, S., Moreau, M., Gélinau, A., Marcelin, G., Magréau-Davy, E., Ouhachi, M., Lesnik, P., et al. (2020). Impaired Kupffer cell self-renewal alters the liver response to lipid overload during non-alcoholic steatohepatitis. *Immunity* 53, 627–640.e5. <https://doi.org/10.1016/j.immuni.2020.06.003>.
- Utz, S.G., See, P., Mildnerberger, W., Thion, M.S., Silvin, A., Lutz, M., Ingelfinger, F., Rayan, N.A., Lelios, I., Buttgerit, A., et al. (2020). Early fate defines microglia and non-parenchymal brain macrophage development. *Cell* 181, 557–573.e18. <https://doi.org/10.1016/j.cell.2020.03.021>.
- van de Laar, L., Saelens, W., De Prijck, S., Martens, L., Scott, C.L., Van Isterdael, G., Hoffmann, E., Beyaert, R., Saeys, Y., Lambrecht, B.N., and Guillems, M. (2016). Yolk sac macrophages, fetal liver, and adult monocytes can colonize an empty niche and develop into functional tissue-resident macrophages. *Immunity* 44, 755–768. <https://doi.org/10.1016/j.immuni.2016.02.017>.
- Van Hove, H., Pombo Antunes, A.R., De Vlamincq, K., Scheyltjens, I., Van Ginderachter, J.A., and Movahedi, K. (2020). Identifying the variables that drive tamoxifen-independent CreERT2 recombination: implications for microglial fate mapping and gene deletions. *Eur. J. Immunol.* 50, 459–463. <https://doi.org/10.1002/eji.201948162>.
- Van Hove, H., Martens, L., Scheyltjens, I., De Vlamincq, K., Pombo Antunes, A.R., De Prijck, S., Vandamme, N., De Schepper, S., Van Isterdael, G., Scott, C.L., et al. (2019). A single-cell atlas of mouse brain macrophages reveals unique transcriptional identities shaped by ontogeny and tissue environment. *Nat. Neurosci.* 22, 1021–1035. <https://doi.org/10.1038/s41593-019-0393-4>.
- Wendeln, A.C., Degenhardt, K., Kaurani, L., Gertig, M., Ulas, T., Jain, G., Wagner, J., Häsler, L.M., Wild, K., Skodras, A., et al. (2018). Innate immune memory in the brain shapes neurological disease hallmarks. *Nature* 556, 332–338. <https://doi.org/10.1038/s41586-018-0023-4>.
- Yamasaki, R., Lu, H., Butovsky, O., Ohno, N., Rietsch, A.M., Cialic, R., Wu, P.M., Doykan, C.E., Lin, J., Cotleur, A.C., et al. (2014). Differential roles of microglia and monocytes in the inflamed central nervous system. *J. Exp. Med.* 211, 1533–1549. <https://doi.org/10.1084/jem.20132477>.
- Yona, S., Kim, K.-W., Wolf, Y., Mildner, A., Varol, D., Breker, M., Strauss-Ayali, D., Viukov, S., Guillems, M., Misharin, A., et al. (2013). Fate mapping reveals origins and dynamics of monocytes and tissue macrophages under homeostasis. *Immunity* 38, 79–91. <https://doi.org/10.1016/j.immuni.2012.12.001>.
- Zhou, Y., Zhou, B., Pache, L., Chang, M., Khodabakhshi, A.H., Tanaseichuk, O., Benner, C., and Chanda, S.K. (2019). Metascape provides a biologist-oriented resource for the analysis of systems-level datasets. *Nat. Commun.* 10, 1523. <https://doi.org/10.1038/s41467-019-09234-6>.

STAR★METHODS

KEY RESOURCES TABLE

REAGENT or RESOURCE	SOURCE	IDENTIFIER
Antibodies		
Chicken anti-GFP (IHC) Fluorophore: unlabeled, polyclonal	Abcam	Cat#: ab13970; RRID: AB_300798
Goat anti-chicken IgY, H+L (IHC) Fluorophore: AF488, polyclonal	Invitrogen	Cat#: A11039; RRID: AB_2534096
Goat anti-mouse IgG1, γ 1 (IHC) Fluorophore: AF546, polyclonal	Invitrogen	Cat#: A21123; RRID: AB_2535765
Goat anti-rat IgG, H+L (IHC) Fluorophore: AF555, polyclonal	Invitrogen	Cat#: A21434; RRID: AB_2535855
Goat anti-rat IgG, H+L (IHC) Fluorophore: AF647, polyclonal	Invitrogen	Cat#: A21247; RRID: AB_141778
Donkey anti-rabbit IgG, H+L (IHC) Fluorophore: AF647, polyclonal	Invitrogen	Cat#: A31573; RRID: AB_2536183
Mouse anti-pan cytokeratin (IHC) Fluorophore: unlabeled, Clone: C-11	Abcam	Cat#: ab7753; RRID: AB_10674321
Rabbit anti-mouse/rat/human Iba1 (IHC) Fluorophore: unlabeled, polyclonal	Wako	Cat#: 019-1974; RRID: AB_839504
Rabbit anti-mouse/rat/human Ki67 (IHC) Fluorophore: unlabeled, Clone: SP6	Abcam	Cat#: 16667; RRID: AB_302459
Rabbit anti-VSG (IHC) Fluorophore: unlabeled, polyclonal	Generated in house	N/A
Rat anti-mouse CD11b (FACS) Fluorophore: BV750, Clone: M1/70	BD Biosciences	Cat#: 746910; RRID: AB_2871704
Rat anti-mouse/human CD11b (FACS) Fluorophore: PE/cy7, Clone: M1/70	BioLegend	Cat#: 101216; RRID: AB_312799
Rat anti-mouse CD16/32, TruStain FcX (FACS) Unlabeled, Clone: 93	BioLegend	Cat#: 101319; RRID: AB_1574973
Rat anti-mouse CD206 (MMR) (FACS) Fluorophore: AF647, Clone: C068C2	BioLegend	Cat#: 141712; RRID: AB_10900420
Rat anti-mouse CD206 (MMR) (FACS) Fluorophore: BV605, Clone: C068C2	BioLegend	Cat#: 141721; RRID: AB_2562340
Rat anti-mouse CD206 (MMR) (FACS) Fluorophore: FITC, Clone: C068C2	BioLegend	Cat#: 141704; RRID: AB_10901166
Rat anti-mouse CD24 (FACS) Fluorophore: PE/cy7, Clone: M1/69	BioLegend	Cat#: 101822; RRID: AB_756048
Rat anti-mouse CD31 (IHC) Fluorophore: unlabeled, Clone: MEC13.3	BD Pharmingen	Cat#: 550274; RRID: AB_393571
Rat anti-mouse CD371 (CLEC12A) (FACS) Fluorophore: PE, Clone: 5D3	BioLegend	Cat#: 143404; RRID: AB_11126984
Rat anti-mouse CD43 (FACS) Fluorophore: BUV737, Clone: S7	BD Biosciences	Cat#: 612840; RRID: AB_2870162
Rat anti-mouse CD43 (FACS) Fluorophore: BV510, Clone: S7	BD Biosciences	Cat#: 563206; RRID: AB_2738069
Rat anti-mouse CD45 (FACS) Fluorophore: APC/cy7, Clone: 30-F11	BioLegend	Cat#: 103116; RRID: AB_312981
Rat anti-mouse CD45 (FACS) Fluorophore: BUV805, Clone: 30-F11	BD Biosciences	Cat#: 748370; RRID: AB_2872789
Rat anti-mouse CD45 (FACS) Fluorophore: BV421, Clone: 30-F11	BioLegend	Cat#: 103134; RRID: AB_2562559

(Continued on next page)

Continued

REAGENT or RESOURCE	SOURCE	IDENTIFIER
Rat anti-mouse CD54 (ICAM-1) (IHC) Fluorophore: unlabeled, Clone: YN1/1.7.4	eBioscience	Cat#: 14-0541-82; RRID: AB_467301
Mouse anti-mouse CX3CR1 (FACS) Fluorophore: BV421, Clone: SA011F11	BioLegend	Cat#: 149023; RRID: AB_2565706
Mouse anti-mouse CX3CR1 (FACS) Fluorophore: PE, Clone: SA011F11	BioLegend	Cat#: 149006; RRID: AB_2564315
Rat anti-mouse F4/80 (FACS) Fluorophore: APC-R700; Clone: T45-2342	BD Biosciences	Cat#: 565787; RRID: AB_2869711
Rat anti-mouse F4/80 (IHC) Fluorophore: unlabeled, Clone: A3-1	Bio-Rad	Cat#: MCA497GA; RRID: AB_323806
Rat anti-mouse GPNMB (FACS) Fluorophore: eFluor660, Clone: CTSREVL	eBioscience	Cat#: 50-5708-82; RRID: AB_2574239
Rat anti-mouse I-A/I-E (FACS) Fluorophore: APC, Clone: M5/114.15.2	BioLegend	Cat#: 107614; RRID: AB_313329
Rat anti-mouse I-A/I-E (FACS) Fluorophore: BUV395, Clone: 2G9	BD Biosciences	Cat#: 743876; RRID: AB_2741827
Rat anti-mouse I-A/I-E (FACS) Fluorophore: PerCP/cy5.5, Clone: M5/ 114.15.2	BioLegend	Cat#: 107626; RRID: AB_2191071
Rat anti-mouse Ly-6B.2 (FACS) Fluorophore: AF647, Clone: 7/4	Bio-Rad	Cat#: MCA771A647; RRID: AB_322437
Rat anti-mouse Ly-6C (FACS) Fluorophore: APC/cy7, Clone: AL-21	BD Pharmingen	Cat#: 560596; RRID: AB_1727555
Rat anti-mouse Lyve1 (IHC) Fluorophore: unlabeled, Clone: ALY7	eBioscience	Cat#: 14-0443-82; RRID: AB_1633414
Chemicals, peptides, and recombinant proteins		
7-amino-actinomycin D (7-AAD)	BioLegend	Cat#: 420404; CAS: 7240-37-1
Actinomycin D	Sigma-Aldrich	Cat#: A1410; CAS: 50-76-0
Alsever's solution	Sigma-Aldrich	Cat#: A3551
β -mercaptoethanol	Sigma-Aldrich	Cat#: M6250; CAS: 60-42-2
Bovine serum albumin (BSA)	ThermoFisher Scientific	Cat#: AM2616; CAS: 9048-46-8
Collagenase type I	Worthington	Cat#: LS004216; CAS: 9001-12-1
Collagenase type IV	Worthington	Cat#: LS004209; CAS: 9001-12-1
Corn oil	Sigma-Aldrich	Cat#: C8267; CAS: 8001-30-7
DAPI	Sigma-Aldrich	Cat#: D9542; CAS: 28718-90-3
Diphtheria toxin	Sigma-Aldrich	Cat#: D0564
DNase I	Roche	Cat#: 04536282001; CAS: 9003-98-9
Ethylenedinitrilotetraacetic acid (EDTA) disodium dihydrate	Duchefa	Cat#: E0511; CAS: 6381-92-6
Fetal calf serum (FCS), heat-inactivated	Gibco	Cat#: 16000044
FITC-dextran, 4kDa	Sigma-Aldrich	Cat#: FD4; CAS: 60842-46-8
Gelatine	Sigma-Aldrich	Cat#: 04055; CAS: 9000-70-8
Hanks' buffered salt solution (HBSS), 1x	Gibco	Cat#: 14175-129

(Continued on next page)

Continued

REAGENT or RESOURCE	SOURCE	IDENTIFIER
L-glutamine	Gibco	Cat#: 25030081; CAS: 56-85-9
Minimum essential medium non-essential amino acids	Gibco	Cat#: 11140035
Melarsoprol	WHO	CAS: 494-79-1
Mowiol	Polysciences Inc.	Cat#: 17951; CAS: 9002-89-5
Normal donkey serum (NDS)	Sigma-Aldrich	Cat#: D9663
Paraformaldehyde (PFA)	Sigma-Aldrich	Cat#: 818715; CAS: 30525-89-4
Penicillin-Streptomycin	Gibco	Cat#: 15140122
Percoll	Cytiva	Cat#: 17-0891-01
PLX3397	Advanced ChemBlocks Inc.	Cat#: H-8970; CAS: 1029044-16-3
Polyethylene glycol (PEG)	Sigma-Aldrich	Cat#: 91893; CAS: 25322-68-3
Rhodamine B isothiocyanate (RBITC)	Sigma-Aldrich	Cat#: 283924; CAS: 36877-69-7
Roswell Park Memorial Institute (RPMI)	Gibco	Cat#: 52400025
Sodium azide	Sigma-Aldrich	Cat#: 199931; CAS: 26628-22-8
Sodium pyruvate	Gibco	Cat#: 11360039; CAS: 113-24-6
Tamoxifen	Sigma-Aldrich	Cat#: T5648; CAS: 10540-29-1
Tissue-Tek O.C.T	Sakura Finetek	Cat#: 4583
TRITC-dextran, 10kDa	ThermoFisher Scientific	Cat#: D1868
Triton	Sigma-Aldrich	Cat#: X100; CAS: 9002-93-1

Critical commercial assays

Annexin V Apoptosis Detection kit	Invitrogen	Cat#: BMS500FI-300
Bio-Plex cytokine assay	BioRad	Cat#: M60009RDPD
Chromium i7 Multiplex kit	10x Genomics	Cat#: PN-120262
Chromium Next Gem Single Cell 3' Gel Bead and Library kit v3.1	10x Genomics	Cat#: PN-1000121
DynaBeads MyOne Silane Beads	ThermoFisher Scientific	Cat#: 37002D
GemCode Single Cell 3' Gel Bead and Library kit v2	10x Genomics	Cat#: PN-120237
SPRIselect Reagent Kit	Beckman Coulter	Cat#: B23318

Deposited data

Raw and analyzed data	This paper	GEO: GSE212078
-----------------------	------------	----------------

Experimental models: Organisms/strains

<i>Trypanosoma brucei brucei</i> AnTat1.1E	N. Van Meivenne (Institute for Tropical Medicine, Belgium)	N/A
Mouse: C57BL/6J	Janvier Labs	IMSR_JAX:000664
Mouse: <i>Cx3cr1</i> ^{CreER}	Goldmann et al. (2013) ; Yona et al. (2013)	IMSR_JAX:020940
Mouse: <i>Cx3cr1</i> ^{GFP/+}	Jung et al. (2000)	IMSR_JAX:005582
Mouse: <i>Flt3</i> ^{Cre}	Benz et al. (2008)	IMSR_EM:11790
Mouse: <i>Lyz2</i> ^{GFP}	Faust et al. (2000)	MGI: 2654932
Mouse: R26-DTR	Buch et al. (2005)	IMSR_JAX:007900
Mouse: R26-YFP	Srinivas et al. (2001)	IMSR_JAX:006148

(Continued on next page)

Continued

REAGENT or RESOURCE	SOURCE	IDENTIFIER
Mouse: <i>Sall1</i> ^{CreER/+}	Inoue et al. (2010)	MGI: 4443031
Software and algorithms		
Adobe Photoshop	Adobe	RRID: SCR_014199
AnalyzeSkeleton plugin	Arganda-Carreras et al. (2010)	https://github.com/fiji/AnalyzeSkeleton
BioRender app	BioRender	RRID: SCR_018361
Cell Ranger mkfastq	10x Genomics	RRID: SCR_017344
Cell Ranger count	10x Genomics	RRID: SCR_017344
CLij2 plugin	Haase et al. (2020)	https://clij.github.io/
DropletUtils package	Lun et al. (2019)	https://github.com/MarioniLab/DropletUtils/
Fiji (ImageJ)	Schindelin et al. (2012)	RRID: SCR_002285
FlowJo	Tree Star Inc.	RRID: SCR_008520
G*Power	Faul et al. (2007)	RRID: SCR_013726
GraphPad Prism	Graph Pad Software Inc.	RRID: SCR_002798
Harmony	Korsunsky et al. (2019)	https://github.com/immunogenomics/harmony
Metascape	Zhou et al. (2019)	RRID: SCR_016620
MorphoLibJ plugin	Legland et al. (2016)	https://github.com/ijpb/MorphoLibJ
R studio		RRID: SCR_000432
Rollin Ball Background Subtraction plugin	Sternberg (1983)	https://github.com/nearlyfreeapps/Rolling-Ball-Algorithm
Seurat package	Satija et al. (2015)	RRID: SCR_016341
Scater package	McCarthy et al. (2017)	RRID: SCR_015954
Skeletonize3D plugin	Lee et al. (1994)	https://github.com/fiji/Skeletonize3D
Triwise package	van de Laar et al. (2016)	https://github.com/saeyslab/triwise
Zen Black	Zeiss	RRID: SCR_013672
Other		
scRNA-seq datasets, gene-cell count matrices and cell annotation matrices	This paper	www.brainimmuneatlas.org
Example code used for scRNA-seq analyses	Pombo Antunes et al. (2021); Scheyltjens et al. (2022)	https://github.com/Movahedilab/

RESOURCE AVAILABILITY

Lead contact

Further information and requests for resources should be directed to and will be fulfilled by the lead contact, Kiavash Movahedi (kiavash.movahedi@vub.be).

Materials availability

This study did not generate new unique reagents.

Data and code availability

All scRNA-seq datasets described in this article are accessible through our interactive webserver at www.brainimmuneatlas.org as of the date of publication. All gene-cell count matrices and cell annotation matrices are available for download via the link. This tool also allows to evaluate the expression of genes and to download DE gene lists. Furthermore, all raw data and gene-cell count matrices have been deposited at GEO (NCBI) and are publicly available as of the date of publication. Accession numbers are listed in the [key resources table](#). All other data that support the findings reported in this study will be shared by the [lead contact](#) upon reasonable request.

Example codes used for scRNA-seq analysis in this paper are available at <https://github.com/Movahedilab/>.

Any additional information required to reanalyze the data reported in this paper is available from the [lead contact](#) upon request.

EXPERIMENTAL MODEL AND SUBJECT DETAILS

Mice

C57BL/6J mice were purchased from Janvier Labs. *Cx3cr1*^{CreER} (Goldmann et al., 2013; Yona et al., 2013), *Cx3cr1*^{GFP/+} (Jung et al., 2000), *Flt3*^{Cre} (Benz et al., 2008), *Lyz2*^{GFP} (Faust et al., 2000), R26-DTR (Buch et al., 2005), R26-YFP (Srinivas et al., 2001) and *Sall1*^{CreER/+} (Inoue et al., 2010) mice were bred in house. Age and sex of the mice are specified in Table S3. All used mouse strains were immunocompetent and housed in standard cages under standard conditions (light/dark 12h/12h, temperature 20–24°C, humidity 45–65%, environmental enrichment). Food and water were provided ad libitum. Animals were checked daily on an individual basis and health status was recorded in a logbook. Body condition score, mobility, posture and (grooming) behavior were carefully monitored and upon abnormal observation, researchers were notified and appropriate action (treatment or euthanasia) was taken. All experiments were approved by the Ethische Commissie Dierproeven at Vrije Universiteit Brussel and performed in accordance with the guidelines set by the Belgian Council for Laboratory Animal Science.

Parasites

Clonal pleomorphic *Trypanosoma brucei brucei* AnTat1.1E parasite stocks were available at -80°C in house (initially received from N. Van Meivenne, Institute for Tropical Medicine, Belgium) and expanded when needed. Hereto, a stock vial of *T. b. brucei* parasites was used to infect C57BL/6 mice (see method details). Around the first blood parasitemia peak (4–6d p.i.), the mice were sacrificed and blood was collected via cardiac puncture. New stocks were obtained by diluting the heparinized blood to a 1:1 ratio in 20% glycerol-containing Alsever's solution (Sigma-Aldrich), aliquoted and stored at -80°C until needed.

METHOD DETAILS

Tamoxifen treatment

Tamoxifen (Sigma-Aldrich) was dissolved in corn oil (Sigma-Aldrich) at a concentration of 20 mg ml⁻¹ while shaking the solution for at least 4 hours at 37°C in the dark. At 3–4 weeks of age, *Cx3cr1*^{CreER}:R26-YFP, *Sall1*^{CreER}:R26-YFP and *Cx3cr1*^{CreER}:R26-DTR mice were injected with the tamoxifen-in-oil solution to induce Cre-mediated recombination. 50 µl was subcutaneously injected near each limb (total of 200 µl), while mice were kept under general anaesthesia. Injections were performed three times, with a 2–3 day interval in between the injections.

Parasite infection

Frozen parasite-in-blood samples (see experimental model and subject details) were thawed and diluted in 1x Hanks' buffered salt solution (HBSS, Gibco) to a final concentration of 2.5 × 10⁴ parasites ml⁻¹. Subsequently, 6-to-10-week-old mice were intraperitoneally injected with 5000 parasites. Successful infection was verified at d6 p.i. via parasitemia counting in a blood sample (see below).

Diphtheria toxin treatment

To achieve brain resident macrophage depletion during the infection, *Cx3cr1*^{CreER}:R26-DTR mice were intraperitoneally injected with 500 ng diphtheria toxin (Sigma-Aldrich) dissolved in 100 µl 1xHBSS during three consecutive days at early or late stage of the disease; one day later the mice were killed and CSF or brain regions were analyzed.

Melarsoprol treatment

To resolve infection, C57BL/6J or *Cx3cr1*^{CreER}:R26-YFP mice were treated intraperitoneally with 10–12 mg kg⁻¹ of the anti-parasitic drug Melarsoprol (received from WHO/Sanofi) in 1:1 polyethylene glycol (PEG, Sigma-Aldrich) :H₂O for four consecutive days, starting at d28 p.i. One week after the first injection, the mice were given two additional injections over two consecutive days. Successful curing was assessed by repeatedly monitoring and confirming the absence of parasites in the blood.

Blood and CSF isolation

Blood was collected via the tail vein and diluted 200 times in Roswell Park Memorial Institute (RPMI) 1640 medium (Gibco). CSF was collected from deeply anesthetized mice via cisterna magna puncture, using pulled glass capillaries (Sutter Instrument co.). Blood-free CSF samples were kept on ice undiluted for parasitemia counts and cytokine measurements, or resuspended in FACS buffer for flow cytometry (see below). Blood-contaminated CSF samples were excluded from analyses.

Single cell isolation from brain (regions)

Single cell isolations were performed as previously described by our group (Van Hove et al., 2019; Scheyltjens et al., 2022). Mice were deeply anesthetized, transcardially perfused with 20 ml of ice-cold phosphate buffered saline (PBS, made in house) and decapitated. For whole brain single cell isolation, brains were dissected and placed in ice-cold RPMI. Brains were cut into small pieces and enzyme mix (30 U ml⁻¹ DNase I, Roche; 10 U ml⁻¹ collagenase type I, Worthington; 400 U ml⁻¹ collagenase type IV, Worthington; diluted in 1xHBSS) was added to allow tissue dissociation. After a 20 min incubation at 37°C, brains were crushed with a syringe plunger and heavily triturated using standard serological pipettes. Next, the samples were filtered twice over 100 µm pore nylon filters and subsequently centrifuged (500 g, 7 min, 4°C). Pellets were resuspended in 5 ml of a 70% standard isotonic Percoll (Cytiva) (SIP) in

1xHBSS solution, and a density gradient was created by gently overlaying the sample with 5 ml of 37% SIP and 5 ml of 30% SIP solution. Following centrifugation (800 g, 30 min, 4°C, minimal acceleration and brake), myelin was removed and the 70%/37% SIP interface containing immune cells was collected and centrifuged (650 g, 5 min, 4°C). Finally, pellets were resuspended in fluorescent activated cell sorter (FACS) buffer (2 mM EDTA, Ducheфа; 2% heat-inactivated fetal calf serum (FCS), Gibco; dissolved in 1xHBSS).

For single cell isolations of brain border regions and hippocampus, the dorsal part of the skull was carefully removed and the dura mater was peeled off of the skull cap. Leaving the dorsal part of the brain exposed, next, a thin section (ca. 1 mm thick) of the dorsal cortex was sliced off using a 0.25 mm low-profile disposable blade 918 (Leica BioSystems) to enrich for subdural meninges cells. Subsequently, the fourth and lateral brain ventricles were exposed and CPs were micro-dissected. Finally, the hippocampus was isolated. All tissues were placed on ice-cold RPMI and digested with enzyme mix over a period of 30 min (37°C), while thoroughly cutting and resuspending the samples every 10 min. The samples were filtered and centrifuged (450g, 6 min for dura and CP; 500 g, 7 min for subdura and hippocampus; 4°C). Subsequently the pellets of dura and CP were resuspended in FACS buffer. Pellets of the subdural meninges were resuspended in 30% SIP solution and centrifuged (800 g, 30 min, 4°C, minimal acceleration/brake). Myelin was removed, subdura and hippocampus samples were washed (650 g, 5 min, 4°C) and pellets were finally also resuspended in FACS buffer.

Parasitemia counts

Parasitemia in blood and brain was quantified through manual counting, using a Neubauer counting chamber. In blood and CSF, parasites were counted immediately after fluid collection. In dura, subdura, CP and hippocampus, parasitemia was only assessed once single cell suspensions were obtained.

Immunohistochemistry

Brain cryosections for immunohistochemistry were obtained as previously described by [Van Hove et al. \(2019\)](#). Mice were deeply anesthetized and transcardially perfused with 10 ml PBS and 20 ml 4% paraformaldehyde (PFA, Sigma-Aldrich)-in-PBS solution. Brains were dissected and post-fixed for 4 hours in ice-cold 4% PFA/PBS. Next, the brains were dehydrated overnight in 15% sucrose-containing PBS (w/v) and subsequently overnight in 30% sucrose-containing PBS (w/v). Finally, the brains were embedded in Tissue-Tek O.C.T (Sakura Finetek) and frozen using dry ice. Cryosections of 12 μm were made using a Leica CM 1850 UV. Sections were washed three times with PBS and blocked for 2 hours at room temperature with 10% normal donkey serum (NDS, Sigma-Aldrich) in PBS containing 3% Triton (Sigma-Aldrich) (PBS-T). Subsequently the sections were stained with primary antibodies in 3% NDS/PBS-T (overnight, 4°C). The following day, the samples were washed three times with PBS-T, and stained with secondary antibodies in 3% NDS/PBS-T (1.5 h, room temperature). The primary and secondary antibodies that were used are listed in the [key resources table](#). Next, the sections were washed three times with PBS-T and once with PBS. The slides were stained with DAPI (Sigma-Aldrich)/PBS solution for 10 min at room temperature and washed twice with PBS. Finally, the sections were mounted using Mowiol® 4-88 (Polysciences Inc.) coverslip mounting solution (prepared according to the manufacturer's instructions) and stored at 4°C.

To obtain wholemounts of dural and subdural meninges, following transcardial perfusion, the dorsal part of the mouse skull was cut open and the skull cap containing the dura mater was placed in ice-cold 4% PFA/PBS for 2 hours. A piece of dorsal subdural meninges was sliced off using a 0.25 mm low-profile disposable blade 918 (Leica BioSystems), and placed in ice-cold 4% PFA/PBS for 2 hours as well. After post-fixation, the dura was carefully removed from the skull cap and both dura and subdural meninges were transferred to PBS. Subsequent steps of washing, staining with primary, secondary antibodies and DAPI, and mounting was performed similarly as for the cryosections.

Images of brain cryosections and meningeal whole mounts were taken using an LSM710 or LSM800 confocal microscope. Images were collected using ZEN black (Zeiss) and processed in Fiji (ImageJ) or Photoshop (Adobe).

Morphology quantification of BAMs

3D analysis was performed using an ImageJ custom macro in Fiji. First, background was subtracted using the Rolling Ball Background Subtraction plugin. Subsequently, a median filter and an automatic threshold were applied using CLIJ2 and the IJ-iso method. Connected component labeling was performed to label different binary components, and small ones were filtered out. Next, skeletonization of the cells was performed using the Skeletonize3D plugin. Finally, the skeletons were analyzed using the AnalyzeSkeleton, 3D Marker Controlled Watershed and MorphoLibJ plugins, to extract the distinct morphological parameters and values.

Serial 2-photon tomography

Lyz2^{GFP} mice (1 naive and 3 late stage infected (d34-36 p.i.)) were deeply anesthetized and subsequently transcardially perfused with 40 ml PBS, 40 ml 4% PFA/PBS and 20 ml heated (35-40°C) rhodamine B isothiocyanate (RBITC, Sigma-Aldrich)-containing gelatine (Sigma-Aldrich) solution, prepared according to the instructions of TissueVision Inc. Next, the animals were placed at a 30° angle, head down, submerged into ice for 30 minutes. The brains were carefully removed, post-fixed in 4% PFA/PBS overnight, and finally transferred into PBS containing 0.1% sodium azide (Sigma-Aldrich). TissueVision Inc. performed serial two-photon tomography ([Ragan et al., 2012](#)) and quantified GFP signal distribution across different brain regions. Thereto, vascular labelling (RBITC) and GFP signal were primarily isolated to different channels. Background autofluorescence and minor bleed-through between the channels was detected and corrected for, and a global threshold was defined and applied to the resulting images to mask GFP^{bright} signal pixels of interest. Next, the Allen Institute Common Coordinate Framework (CCF) was warped onto a 10% downsampled dataset

of our brain samples, using a course-to-fine registration consisting of translation, affine and non-linear deformations. GFP^{bright} signal density—defined as the total number of GFP^{bright} pixels/total number of region pixels across all coronal sections in the sample—was calculated for a defined subset (358; see [Table S2](#)) of the CCF-annotated regions and region groups (>600). The quantitative results in [Figure S3D](#), are the top 36 regions that showed infiltration of GFP^{bright} cells, i.e. those regions with a GFP^{bright} pixel to region pixel ratio above 10% in at least one of three infected mice. Images were processed in Fiji (ImageJ), and the corresponding areas of interest were highlighted on coronal sections/pictograms that were downloaded from the Allen brain atlas (<https://mouse.brain-map.org/static/atlas>) and adapted in Adobe Photoshop.

Assessment of brain barrier leakage

Mice were injected intravenously with 100 μ l of either FITC-dextran (4 kDa, Sigma-Aldrich) or lysine-fixable TRITC-dextran (10 kDa, ThermoFisher Scientific) in 1xHBSS, at a concentration of 18.75 mg ml⁻¹. For the quantification of leakage at the blood-CSF barrier, mice were deeply anesthetized 15 min after FITC-dextran injection, and CSF was collected as described above. Next, CSF samples were centrifuged (650g, 4°C, 5 min) and supernatant was stored at -80°C. CSF samples were diluted 20 to 50 times (depending on the experiment) in 1xHBSS, and relative fluorescence was measured at $\lambda_{ex}/\lambda_{em}=488/520$ nm. For the visualization of leakage at the blood-brain barrier, mice were deeply anesthetized 1 hour after TRITC-dextran injection, and brains were dissected and post-fixed for 24 hours in 4% PFA/PBS solution. Subsequently, the brains were dehydrated, frozen, cut into cryosections and stained as described above. Cryosections were imaged and processed as described above.

Cytokine measurements in CSF

CSF was collected as described above and centrifuged (650 g, 6 min, 4°C). Cytokine levels in the supernatant were measured using the Bio-Plex cytokine assay (BioRad) in accordance with the manufacturer's instructions. Among the 23 tested cytokines (IL1 α , IL1 β , IL2, IL3, IL4, IL5, IL6, IL9, IL10, IL12p40, IL12p70, IL13, IL17, MCP1/CCL2, MIP1 α /CCL3, MIP1 β /CCL4, RANTES/CCL5, Eotaxin/CCL11, KC/CXCL1, G-CSF, GM-CSF, IFN γ , TNF α), only the ones that showed a significant concentration difference upon infection, were included in the results of this manuscript.

Flow cytometry and cell sorting

For multicolor flow cytometry, single cell suspensions were stained with Zombie Aqua Fixable Live-dead (BioLegend) following the manufacturer's instructions. Next, the samples were blocked with rat anti-mouse CD16/CD32 (clone 2.4G2, made in house) for 15 min on ice, and subsequently stained for 20 min on ice, using the antibodies listed in the [key resources table](#). Finally, samples were washed with FACS buffer and measured on a BD FACS Canto II or BD FACSymphony A3 flow cytometer. The obtained data was analyzed using FlowJo (v10.7.1 and v10.8.1) or Cytobank (<https://www.cytobank.org>).

For scRNA-seq, single cell suspensions were blocked with rat anti-mouse CD16/CD32 for 15 min on ice, and subsequently stained for 20 min on ice. The antibodies used for staining varied over the different experiments. For the comparison between naive and infected whole brain, we used anti-CD45-APC/cy7, anti-CD11b-PE/cy7 and anti-CX3CR1-PE, to allow sorting of microglia and myeloid infiltrates. In the other experiments, we sorted all myeloid cells, and stained only with anti-CD45-APC/cy7 (or BV421 fluorophore) and anti-CD11b-PE/cy7. Note, for the cured versus control samples of the borders, blocking and staining was simultaneously performed for 30 min on ice, in 25 μ l PBS + 0.04% bovine serum albumin (BSA, ThermoFisher Scientific) staining buffer (instead of FACS buffer), containing mouse TruStain FcX (BioLegend), the anti-CD45-APC/cy7 and anti-CD11b-PE/cy7 antibodies, and a panel of 174 oligo-conjugated mouse cell surface protein antibodies as previously described ([Pombo Antunes et al., 2021](#)). Subsequently, the samples were washed and 7-AAD (BioLegend) or DAPI (Sigma-Aldrich) was used to label dead cells. The appropriate cells were sorted on a BD FACS Aria II instrument using a 85 μ m nozzle, and collected in ME medium (RPMI supplemented with 10% (v/v) heat-inactivated FCS, 300 μ g ml⁻¹ L-glutamine (Gibco), 100 U ml⁻¹ penicillin, 100 μ g ml⁻¹ streptomycin (Gibco), 1% 100mM pyruvate (100x) (Gibco), 1% minimum essential medium non-essential amino acids (100x) (Gibco) and 1% β -mercaptoethanol (Sigma-Aldrich)). The complete dissociation and sorting protocol took approximately 3-3.5 hours for whole brain samples and 2.5-3 hours for border regions. Finally, the sorted samples were centrifuged (450 g, 6 min, 4°C) and resuspended in PBS + 0.04% BSA to an estimated concentration of 1000 cells μ l⁻¹.

Assessment of apoptosis via flow cytometry

To detect apoptotic cell death, whole brain samples were processed into single cell suspensions, stained and measured by flow cytometry as described above. However, a few adaptations were made to the protocol. Density gradient centrifugation was performed with only 30% SIP solution rather than 30%/37%/70% SIP solution, in order to avoid loss of dead cells in the other gradient fractions whilst still being able to segregate cells from myelin debris. Prior to blocking, cells were washed with 1xHBSS and resuspended in 1x Binding buffer as recommended by the manufacturer (Invitrogen). Antibody and AnnexinV (Invitrogen) staining were performed simultaneously (15 min, at room temperature). Next, samples were washed with 1x Binding buffer, and Propidium Iodide (Invitrogen) was added prior to measuring the samples on the flow cytometer.

scRNA-seq using 10x Genomics platform

In each of the experiments, to obtain a sufficient number of cells, samples were pooled. For scRNA-seq comparison between naive and infected mice, we pooled the brains (including border regions) of 4 C57BL/6 mice per condition. Analysis of the CP upon infection

was performed on pooled samples from lateral and fourth ventricle of $n=8$ *Cx3cr1*^{CreERT};R26-YFP mice. Transcriptional dynamics upon resolution of infection was obtained from $n=2-3$ pooled C57BL/6 mouse brains per time point. Lastly, comparison between cured and age-matched control samples was performed on pooled samples of $n=6$ cured and $n=8$ control *Cx3cr1*^{CreERT};R26-YFP mice.

Single cell suspensions of brain and brain border regions were obtained, and cells of interest were sorted as described above. To generate single-cell gel beads in emulsion (GEM), single cell suspensions were loaded on a GemCode Single Cell Instrument (10x Genomics). For most samples, the GEMs and scRNA-seq libraries were prepared with the GemCode Single Cell 3' Gel Bead and Library kit v2 (10x Genomics) and the Chromium i7 Multiplex kit (10x Genomics), according to the manufacturer's instructions. For the cured versus control samples, we used a Chromium Next Gem Single Cell 3' Gel Bead and Library kit v3.1 (10x Genomics). In essence, GEM reverse-transcription was achieved in a 96-deep-well plate by an incubation reaction module at 53°C for 45 min, 85°C for 5 min, finishing at 4°C, generating barcoded complementary DNA (cDNA). Subsequently, GEMs were broken and cDNA was cleaned up with DynaBeads MyOne Silane Beads (ThermoFisher Scientific) and SPRIselect Reagent Kit (Beckman Coulter). Full-length, barcoded cDNA was amplified by a polymerase chain reaction (PCR) in a 96-deep-well reaction module at 98°C for 3 min, 14 cycles of 98°C for 15 s, 67°C for 20 s and 72°C for 1 min, a final cycle at 72°C for 1 min and ending at 4°C. After clean-up using SPRIselect Reagent Kit and enzymatic fragmentation, Illumina-ready sequencing libraries were generated, by library construction through addition of R1 (read 1 primer), P5, P7, i7 sample index and R2 (10x Genomics), via end-repair, A-tailing, adapter ligation, post-ligation SPRIselect cleanup/size selection and sample index PCR. The cDNA content of pre-fragmentation and post-sample index PCR samples was analysed using a 2100 BioAnalyzer (Agilent). The sequencing libraries were loaded onto an Illumina Hi-Seq4000 or an Illumina NovaSeq6000 flow cell, using the sequencing settings recommended by 10x Genomics.

Gene expression data processing

The Cell Ranger pipeline (10x Genomics) was used for sample demultiplexing and to generate FASTQ files for read 1, read 2 and the i7 sample index. Read 2, containing the cDNA, was mapped to the mouse mm10 reference genome using STAR. Next, barcode processing, unique molecular identifier (UMI) filtering and single-cell 3' gene counting was performed using the Cell Ranger suite and Seurat v3.2.2. The average of the mean reads per cell across all libraries was 53675 ± 22645 , and the average sequencing saturation was $74.46 \pm 9.09\%$ (calculated by Cell Ranger). In total 13 individual libraries were created in this study, with a total of 55393 myeloid cells. Low quality cell barcodes associated with empty droplets were filtered out, using the emptyDrops function of the DropletUtils package (v.1.10.1) on the RNA expression data with a FDR threshold of 0.01. The gene expression matrices were further pre-processed and filtered using the Seurat (v3.2.2) and Scater R packages (v.1.18.3). Outlier cells were identified based on three metrics (library size, number of expressed genes and proportion of mitochondrial genes per cell); cells were defined as outliers when for either of the metrics they were three or more median absolute deviations away from the median value (in the lower tail of the distribution for library size and the number of expressed genes, and in the higher tail for proportion of mitochondrial genes) across all cells. Additionally, lowly abundant genes were removed, by calculating the average gene count across all cells and defining a lower limit threshold based on the distribution as previously described (Lun et al., 2016). The raw counts were normalized using the LogNormalize function from the Seurat package, which normalizes the gene expression for each cell by its total count, multiplies it by a scale factor (10 000) and \log_2 -transforms the result. Next, highly variable genes were detected as previously described by Stuart et al. (2019), and the data were scaled per gene by linear transformation. Subsequently, the highly variable genes were used for principal component analysis and unsupervised dimensionality reduction via uniform manifold approximation and projection for dimension reduction (UMAP). Unsupervised clustering was performed using graph-based clustering with the Leiden Algorithm as implemented in the Seurat R package. Of note, for the whole brain dataset of naive versus infected mice and the dataset of CP during infection, a previously described list of dissociation-induced genes (Van Hove et al., 2019) was removed from the highly variable gene list to limit their effect on dimensionality reduction and clustering; these samples were namely not processed in media containing the transcription blocker Actinomycin D (Sigma-Aldrich). This step was not performed for the whole brain cured kinetics dataset, as stress genes appeared to be relevant and clustering results were similar with and without removing dissociation-induced genes, nor in the cured versus control datasets, as these samples were processed with Actinomycin D.

To remove batch effect and technical/biological noise when combining CP data from infected mice with the previously described CP dataset from naive mice (GSM3687214) (Van Hove et al., 2019), we relied on the Harmony algorithm (Korsunsky et al., 2019). Harmony projects cells into a shared embedding, where cells are grouped according to cell type rather than dataset-specific conditions. Soft k-means clustering is performed to assign cells to clusters while favoring a mixed dataset representation, and next, cluster centroids are used to compute cluster-specific linear correction factors that correct the assignment of the cluster-weighted average of each cell. This process is iterated until all cell-to-cluster assignments are stable. Default parameters for Harmony were used, except for theta, which was set to zero. This parameter defines the degree of penalty for dependence between batch and cluster assignment. Higher values of theta favor more independence and result in more diverse clusters, while theta equal to zero does not encourage any diversity. In this case, the corrected Harmony embeddings were used rather than principal components to perform unsupervised clustering of the cells and UMAP dimensionality reduction.

Clustering was visualized in two-dimensional UMAP plots using the Seurat R package. Analysis of differentially expressed (DE) genes between distinct cell clusters was performed using the Seurat FindMarkers function with the Wilcoxon rank-sum test. Adjustment of P-values was performed using Bonferroni correction. Clusters with low expression of *Ptprc* expression, and high expression of fibroblast or endothelial cell marker genes, were identified as non-immune cells and were excluded from the analysis.

YFP transgene expression analysis

To identify cells expressing the YFP transgene, we added the YFP construct sequence to the mouse mm10 reference genome, and used Kallisto v.0.46.0 with default parameters to map the FASTQ files. We filtered the SAM output files from Kallisto for the YFP transcript. The read headers from these filtered SAM files were then mapped to the read 1 (R1) FASTQ file (Cell Ranger mkfastq output) to identify the cell barcode of each YFP read. Finally, to estimate the expression of YFP, we counted the number of times a cell barcode was present, and cells with a cell count equal to or higher than three were considered YFP⁺.

Heatmaps, GO enrichment and triwise plots

Heatmaps highlighting DE genes in different clusters were generated either via the DoHeatmap function in the Seurat R package, which shows scaled expression for a selected number of individual cells per cluster, or using ggplot2 (v.3.3.4).

To predict putative biological functions of blood-recruited macrophages during infection, we performed gene ontology enrichment (GO) analysis based on DE genes between MF1, MF2 and MF3. First, we made DE gene lists for each one of the macrophage clusters, compared to the other two, using an adjusted P value cut-off of 10^{-5} and a $\log_2(\text{FC})$ cut-off of 0.5. For each of the macrophage clusters, these DE genes were inserted into the Metascape online tool (<https://metascape.org>) (Zhou et al., 2019) with default parameters, input and analyzed as *M. musculus* species. The top putative biological functions predicted by Metascape for MF1, MF2 and MF3-specific DE genes are summarized in Table S1.

To visualize potentially relevant functions, we first made a single gene list of all DE genes between the three macrophage clusters (adjusted P value $< 10^{-5}$, $\text{abs}(\log_2\text{FC}) > 0.5$), and then used the Metascape output for the generation of GO term-specific triwise and rose plots, which together highlight directional DE gene expression for enriched GO terms. In the triwise plots every dot represents a single gene, its direction indicates in which macrophage cluster the gene is upregulated and its distance from the center is a measure of the scaled average expression in the distinct clusters (correlates to $\log_2\text{FC}$). Accordingly, genes with similar expression in all three macrophages clusters will lie close to the center, regardless of their absolute expression values. The rose plots show the directional distribution of DE genes that are related to a specific enriched GO term, with the surface of any circle section denoting the relative number of DE genes in a particular direction. The generation of the triwise and rose plots was based on the R Triwise package (v0.99.5) for triwise comparison of bulk RNA-seq data (van de Laar et al., 2016, <https://zouter.github.io/triwise/>). To adapt the workflow to scRNA-seq data analysis, we first calculated the average expression for each gene in MF1, MF2 and MF3 clusters using the AverageExpression Seurat function with input "scale.data". We opted for the use of scaled expression data, as the triwise plots based on unscaled data emphasized highly expressed genes (e.g. ribosomal genes). The average expression matrix was transformed to barycentric coordinates using the transformBarycentric triwise function and used as input for plotting triwise and rose plots.

x,y-representation of gene expression dynamics

To visualize gene expression dynamics over time upon resolution of infection, we defined a function that plots the average scaled expression of a number of genes of interest for a selected subset of cells in function of time post treatment.

Schematic representations using Biorender

Schematic representations of scRNA-seq and fate-mapping experiments were visualized using the Biorender application, and Biorender templates were adapted to make the graphical abstract.

Experimental design

Sample sizes were determined via power analyses in G*Power v3.1.9.2. The number of mice (n) and replicates for each experiment is specified in the figure legends and in Table S3. When experiments were performed across different timepoints post infection/resolution or included distinct experimental groups, mice were randomized based on age and sex; in the absence of age or sex differences, mice were randomly attributed to different experimental groups. Data collection and analysis were not performed blind to the experimental conditions. Trypanosome-injected mice that did not show an infection at d6 p.i., were excluded. CSF samples that were contaminated with blood were not included in the analyses either. For scRNA-seq experiments, primary data exclusion was based on 3 metrics (library size, number of expressed genes and proportion of mitochondrial genes); cells were tagged as outliers and excluded when they were three or more median absolute deviations away from the median value of either of the 3 metrics across all cells. As we were interested in the immune cell compartment, we excluded *Ptprc*-negative cells as well. Otherwise, no data was excluded.

QUANTIFICATION AND STATISTICAL ANALYSIS

All graphs represent mean \pm s.e.m. All statistical calculations (except for scRNA-seq) were performed using GraphPad Prism v8.2.0. Significance was defined as P-values reaching a value below 0.05 (indicated: *), 0.01 (**), 0.001 (***), 0.0001 (****). The statistical parameters and tests that were used are specified in the figure legends and details of the analyses can be found in Table S3. For scRNA-seq, differential expression was assessed using the Wilcoxon rank sum test (two-sided) as implemented in the Seurat R package, and P-value adjustments were performed via Bonferroni correction, based on the total number of genes in the dataset. Data was assumed to be normally distributed, though this was not formally tested.